Global free tropospheric NO$_2$ Abundances Derived using a Cloud Slicing Technique applied to Satellite Observations from the Aura Ozone Monitoring Instrument (OMI)

S. Choi[1,2], J. Joiner[2], Y. Choi[3], B. N. Duncan[2], and E. Bucsela[4]

[1]Science Systems and Applications Inc., Lanham, MD, USA
[2]NASA Goddard Space Flight Center, Greenbelt, MD, USA
[3]University of Houston, Houston, TX
[4]SRI International, Menlo Park, CA, USA

Correspondence to: Sungyeon Choi
(sungyeon.choi@nasa.gov)

Abstract. We derive free-tropospheric NO_2 volume mixing ratios (VMRs) and stratospheric column amounts of NO_2 by applying a cloud slicing technique to data from the Ozone Monitoring Instrument (OMI) on the Aura satellite. In the cloud-slicing approach, the slope of the above-cloud NO_2 column versus the cloud scene pressure is proportional to the NO_2 VMR. In this work, we use a sample of nearby OMI pixel data from a single orbit for the linear fit. The OMI data include cloud scene pressures from the rotational-Raman algorithm and above-cloud NO_2 vertical column density (VCD) (defined as the NO_2 column from the cloud scene pressure to the top-of-the-atmosphere) from a differential optical absorption spectroscopy (DOAS) algorithm. Estimates of stratospheric column NO_2 are obtained by extrapolating the linear fits to the tropopause. We compare OMI-derived NO_2 VMRs with in situ aircraft profiles measured during the NASA Intercontinental Chemical Transport Experiment Phase B (INTEX-B) campaign in 2006. The agreement is generally within the estimated uncertainties when appropriate data screening is applied. We then derive a global seasonal climatology of free-tropospheric NO_2 VMR in cloudy conditions. Enhanced NO_2 in the free troposphere commonly appears near polluted urban locations where NO_2 produced in the boundary layer may be transported vertically out of the boundary layer and then horizontally away from the source. Signatures of lightning NO_2 are also shown throughout low and middle latitude regions in summer months. A profile analysis of our cloud slicing data indicates signatures of uplifted and transported anthropogenic NO_2 in the middle troposphere as well as lightning-generated NO_2 in the upper troposphere. Comparison of the climatology with simulations from the Global Modeling Initiative (GMI) for cloudy conditions (cloud optical thicknesses > 10) shows similarities in the spatial patterns of continental pollution outflow. However, there are also some differences in the seasonal variation of free-tropospheric NO_2 VMRs near highly populated regions and in areas affected by lightning-generated NO_x. Stratospheric column NO_2 obtained from cloud slicing agrees well with other independently-generated estimates, providing further confidence in the free-tropospheric results.

1 Introduction

Tropospheric nitrogen dioxide (NO_2) is mainly produced by fossil fuel combustion, biomass burning, and soil emission near the Earth's surface and by lightning and aircraft emissions in middle and upper troposphere. NO_2 is an important tropospheric constituent, because it is both a pollutant and
30   climate agent. It has adverse effects on human health (Brook et al., 2007) and is one of six criteria pollutants designated by the US Environmental Protection Agency (EPA). It is contributes to the formation of ozone, another EPA criteria pollutant. NO_2 also has both direct and indirect radiative effects. The direct effect results from NO_2 absorption of incoming sunlight in the ultraviolet (UV) and visible (VIS) spectral range (e.g., Solomon et al., 2007; Vasilkov et al., 2009). Because NO_2 is
35   an ozone precursor and affects tropospheric concentrations of methane, it also has indirect short- and long-wave radiative effects (e.g. Fuglestvedt et al., 2008; Wild et al., 2001; Shindell et al., 2009).

     NO_2 has distinct absorption features in the UV/VIS (primarily at blue wavelengths) that can be remotely sensed by satellite spectrometers using Differential Optical Absorption Spectroscopy (DOAS) techniques. For example, tropospheric vertical column densities (VCDs) of NO_2 have
40   been estimated using spectral radiance measurements from the Global Ozone Monitoring Experiment (GOME) (Richter and Burrows, 2002), SCanning Imaging Absorption spectroMeter for Atmospheric CHartographY (SCIAMACHY) (Richter et al., 2005), the Ozone Monitoring Instrument (OMI) (Boersma et al., 2008, 2011; Bucsela et al., 2006, 2008), and the Second Global Ozone Monitoring Experiment (GOME-2) (Munro et al., 2006). The retrieved tropospheric columns of NO_2 have
45   been evaluated with aircraft, ground-based, and balloon measurements. For example, OMI-derived VCDs show moderately good agreement with aircraft measurements from the NASA Intercontinental Chemical Transport Experiment-A (INTEX-A) and -B (INTEX-B) Experiment (Bucsela et al., 2008; Boersma et al., 2008, 2011), ground-based direct-sun DOAS measurements (Herman et al., 2009), and multi-axis DOAS measurements (Celarier et al., 2008; Hains et al., 2010).
50   With their global coverage, satellite tropospheric column estimates have provided important information related to tropospheric NO_x chemistry and transport. Satellite retrievals show decreases of NO_2 tropospheric columns over the United States in recent years (Russell et al., 2012; Duncan et al., 2013) and Europe (Castellanos and Boersma, 2012). These reductions result from emission controls and the economic recession. Reductions in NO_2 were also observed over Beijing and the surround-
55   ing areas during the 2008 olympic and paralympic games (Witte et al., 2009). Lamsal et al. (2013) showed that OMI-derived surface NO_2 concentrations are highly correlated with urban population, but that the NO_2 to population relationship is geographically dependent. Satellite measurements of tropospheric NO_2 columns have also been utilized to study sources and long range transport of NO_x in conjunction with chemical transport models (e.g., Martin et al., 2003, 2006; Zhang et al., 2007;
60   Beirle et al., 2004, 2011; Jaeglé et al., 2005; Frost et al., 2006; Boersma et al., 2008; Lin et al., 2010; Russell et al., 2010). Top-down approaches using satellite measurements provide NO_x source constraints for regional- and global- scale chemical transport models (Martin et al., 2003; Choi et

al., 2008; Lamsal et al., 2010).

There have been only a few studies that have utilized cloudy satellite NO_2 observations, and they have primarily focused on lightning-generated NO_x (e.g., Boersma et al., 2005). Cloudy data are typically discarded in most studies that use satellite-derived tropospheric NO_2 columns, because clouds screen the near-surface from observation. However, the screening property of clouds can be exploited to provide unique estimates of NO_2 concentrations in the free troposphere using cloud-slicing techniques. It is otherwise difficult to separate the boundary layer portion of the NO_2 column from the free-tropospheric contribution. Cloud slicing can also be used to estimate stratospheric NO_2 burdens. Ziemke et al. (2001, 2003, 2005, 2009) pioneered cloud slicing approaches to estimate free tropospheric O_3 concentrations as well as stratospheric column amounts of O_3. The ozone derived from cloud slicing has been validated by extensive comparisons with ozonesondes (Ziemke et al., 2003) and Microwave Limb Sounder (MLS) data (Ziemke et al., 2009). Ziemke et al. (2010) and Ziemke and Chandra (2010) subsequently derived tropospheric and stratospheric ozone climatologies, and Ziemke et al. (2010) developed the ozone El Niño-Southern Oscillation (ENSO) index that has been compared with chemistry-climate simulations (Oman et al., 2013).

Measurements of NO_2 in the free-troposphere are sparse. Aircraft in situ measurements, lidar observations, and balloon-sonde soundings have been confined mainly to field campaigns that are limited in spatial and temporal extents. UV/VIS limb soundings provide vertical profiles of NO_2, but the measurements are limited to the stratosphere (Bovensmann et al., 1999).

Cloud-slicing of NO_2 from satellite measurements can potentially provide additional information about spatial and temporal variations in free tropospheric NO_2 concentrations. Model studies show that lightning NO_x production contributes to free tropospheric NO_2 abundances, but magnitudes and distributions are still largely unknown; in particular, vertical distributions of lightning NO_x are dependent upon the characteristics of the convection parameterizations in the models (Choi et al., 2005, 2008; Allen et al., 2012; Martini et al., 2011). The NO_2 lifetime in the free troposphere (up to a week or more) allows for intercontinental transport of uplifted anthropogenic and lightning-generated NO_2 (e.g., Li et al., 2004; Wang et al., 2006; Zhang et al.,, 2008; Walker et al., 2010). While this transport has been simulated, global NO_2 observations in the free troposphere have not been available for extensive evaluation. In addition, knowledge of the distributions of NO_2 in the free troposphere is important for calculations of its anthropogenic radiative forcing (e.g. Fuglestvedt et al., 2008; Wild et al., 2001; Shindell et al., 2009).

In this study, we use OMI to infer free tropospheric NO_2 VMRs and stratospheric column amounts of NO_2. To derive these quantities, we use the OMI-inferred above-cloud NO_2 columns and cloud parameters from highly cloudy scenes. We evaluate the derived OMI NO_2 VMRs with available aircraft data from the NASA INTEX-B campaign. We derive a global seasonal climatology of free tropospheric NO_2 VMRs from OMI. For reference, we show an example of a comparison with NO_2 fields simulated by a chemical-transport model, the Global Modeling Initiative (GMI). We also con-

100   struct coarse profiles for several regions with sufficient cloud pressure variability. Finally, we infer seasonal, zonal-mean stratospheric column amounts of NO_2 and compare them with independent estimates including simulations from GMI.

2   Data description

2.1   Space-based measurements from OMI

105   OMI is a UV/VIS grating spectrometer that flies aboard the NASA Aura spacecraft (Levelt et al., 2006). Aura is in a sun-synchronous orbit with a local equator crossing time of $13:35 \pm 0:05$ (ascending node). OMI provides daily global coverage with a nadir pixel size of approximately 13×24 km^2 and a swath width of about 2600 km. It has separate channels for UV and VIS observations. The OMI spectral resolutions in the VIS and UV channels are 0.63 and 0.45 nm, respectively. An

110   obstruction outside the instrument (known as the "row anomaly") has reduced the swath coverage starting in May 2008. In order to avoid the row anomaly, we focus on OMI data obtained from 2005–2007.

2.1.1   OMI cloud scene pressure

OMI has two independent cloud retrieval algorithms. They are described in detail by Stammes

115   et al. (2007). Here, we provide a brief explanation of these algorithms. One algorithm uses the collision-induced O_2-O_2 absorption band near 477 nm in the VIS channel; its official product name is OMCLDO2 (Acarreta et al., 2004; Sneep et al., 2008). The other makes use of the filling-in effect of rotational Raman scattering (RRS) at wavelengths from 345 to 354 nm in the UV-2 channel (OMCLDRR) (Joiner and Vasilkov, 2006; Vasilkov et al., 2008).

120   Both algorithms use the Mixed Lambertian Equivalent Reflectivity (MLER) model that accurately reproduces the observed Rayleigh scattering or atmospheric absorption in a cloudy scene (Koelemeijer and Stammes, 1999; Ahmad et al., 2004). The MLER model utilizes the independent pixel approximation; it treats a measured cloudy pixel radiance (I_m) as a weighted sum of two independent subpixels: clear (I_{clr}) and cloudy (I_{cld}). The clear and cloudy subpixels are weighted by an

125   effective cloud fraction (f_c), i.e.,

$$I_m = I_{\mathrm{clr}}(P_{\mathrm{terrain}}) \cdot (1 - f_c) + I_{\mathrm{cld}}(P_c) \cdot f_c, \qquad (1)$$

where P_{terrain} is the terrain pressure and P_c is the cloud optical centroid pressure; P_c can be considered as a reflectance-weighted pressure located inside a cloud (Vasilkov et al., 2008; Joiner et al., 2012). This is distinct from the cloud-top pressure derived from thermal infrared measurements. To

130   model I_{cld} and I_{clr}, clouds and the Earth's surface are treated as Lambertian reflectors (i.e., through which no light is transmitted). For the clear-sky contribution, the surface LER is taken from a precomputed climatology that varies in space and time. The Lambertian clouds are treated as having a

5

fixed albedo of 0.8. In scenes containing transmissive clouds with an overall LER < 0.8, $f_c < 1$; the clear subpixel contribution (first term in the right-hand side of Eq. 1) accounts for light transmitted through the cloud. We also note that f_c is different from the geometric cloud fraction as it is designed to account for cloud transmission within the context of the MLER model. We have found that f_c is practically spectrally invariant over the US/VIS wavelengths considered here. In the OMCLDRR algorithm, f_c is retrieved by inverting Eq. 1 at a wavelength unaffected by RRS. Then P_c is retrieved to be consistent with the observed amount of RRS filling-in.

We also make use of a wavelength-dependent quantity known as the cloud radiance fraction (f_r), defined as the fraction of radiance contributed by clouds (and aerosol). Within the context of the MLER model, f_r is computed as

$$f_r = \frac{I_{\mathrm{cld}}(P_c) \cdot f_c}{I_m}. \tag{2}$$

Cloud optical centroid pressures from OMCLDO2 and OMCLDRR are very similar, particularly for pixels with high values of f_c and f_r (Joiner et al., 2012). However, there are some subtle differences, particularly over the Pacific where there is a high incidence of multi-layer clouds. As a result, cloud slicing NO_2 VMRs derived with the two cloud products exhibit some differences in spatial patterns, particularly over equatorial pacific and Gulf of Mexico. In this work, we use P_c from OMCLDRR. For reference, we show sample results that use OMCLDO2 P_c in Appendix D.

2.1.2 OMI Above-cloud column NO_2

NO_2 slant column densities (SCD) are retrieved from solar backscattered radiances in the VIS channel with a spectral fitting window of 405-465 nm. These data are provided in the OMNO2A product (Boersma et al., 2011). Fitting errors of NO_2 SCDs range from $0.3–1 \times 10^{15}$ cm^{-2}. There is evidence that NO_2 SCDs are positively biased by $\sim 25\%$ (Krotkov, 2013); therefore our estimates from cloud slicing will be biased by the same amount.

Here, we divide the OMI NO_2 SCD by the geometric air mass factor ($AMF_{\mathrm{geometric}}$) to obtain estimates of NO_2 VCDs in highly cloudy conditions. $AMF_{\mathrm{geometric}}$ is given by

$$AMF_{\mathrm{geometric}} = \sec(SZA) + \sec(VZA), \tag{3}$$

where SZA and VZA are the solar and view zenith angles, respectively. $AMF_{\mathrm{geometric}}$ is appropriate for use in an atmosphere where the effects of Rayleigh scattering are relatively small. This is generally the case for highly cloudy observations at NO_2 wavelengths at moderate SZAs.

It is useful at this point to introduce the concept of cloud scene pressure (P_{scene}) given by

$$P_{\mathrm{scene}} = f_r \cdot P_c + (1 - f_r) \cdot P_{\mathrm{terrain}}. \tag{4}$$

The derived NO_2 VCD in a cloudy pixel can be interpreted as the total column from P_{scene} to the top-of-the-atmosphere (i.e., the total column above P_{scene}). Eq. 4 is derived by assuming that the NO_2

6

profile is vertically uniform between P_terrain and P_c (Joiner et al., 2009). Because this condition will not be met for NO_2 in highly polluted regions, here we use only pixels where $f_r > 0.9$. For these pixels, the below-cloud contribution to the observed VCD (i.e., from the second term on the right hand side of Eq. 4) is small and $P_\text{scene} \simeq P_c$. Like P_c, P_scene is located below the physical cloud top

170 altitude. Henceforth we refer to the derived NO_2 VCD in a cloudy scene (NO_2 VCD = NO_2 SCD / $AMF_\text{geometric}$) as the above-cloud NO_2 VCD.

2.1.3   OMNO2B estimates of Stratospheric and Tropospheric NO_2 VCDs

Stratospheric NO_2 VCDs are estimated and reported in the OMNO2B product (Bucsela et al., 2013). We use these estimates as an independent check on our derived stratospheric NO_2 VCDs from cloud

175 slicing. The OMNO2B procedure for estimating stratospheric VCDs is explained in detail by Bucsela et al. (2013). Here we provide a brief explanation of the procedure. First, an initial VCD is obtained by dividing the NO_2 SCD (Sect. 2.1.2) by a stratospheric air mass factor (i.e., the air mass factor is calculated using radiative transfer, assuming that all NO_2 is contained in the stratosphere). Then, the stratospheric VCD is estimated for two cases: (1) In clean areas (with small amounts

180 of tropospheric NO_2), stratospheric VCDs are obtained by subtracting GMI estimates of the tropospheric column from the initial VCD. Spatial smoothing is then applied to the resulting geographic field; (2) Where there is substantial tropospheric NO_2 pollution, the stratospheric VCDs are estimated using spatial interpolation from the surrounding clean regions. Tropospheric NO_2 VCDs are then estimated by taking the differences between the total and stratospheric SCDs and converting

185 them to VCDs using appropriate stratospheric and tropospheric AMFs.

2.2 NO_2 in-situ measurements from NASA DC-8 aircraft during INTEX-B

We evaluate OMI NO_2 cloud slicing results using INTEX-B aircraft in situ NO_2 measurements. INTEX-B was an atmospheric field campaign conducted in the spring of 2006. Its major goals included (1) understanding transport and evolution of Asian pollution and its implications for air

190 quality, and (2) validating space-borne retrievals of tropospheric composition including those from OMI (Singh et al., 2009). INTEX-B NO_2 data were obtained using the University of California at Berkeley Laser-Induced Fluorescence instrument (TD-LIF) on the NASA DC-8 aircraft in 1 second intervals (Thornton et al., 2000; Perring et al., 2010; Bucsela et al., 2008). At 1 Hz, the mixing ratio observations have precisions ranging from ± 23 pptv at 1000 hPa to ± 46 pptv at 200 hPa at a signal

195 to noise ratio of 2.

2.3   GMI model simulation

We use GMI chemical transport model simulations for comparison with our NO_2 cloud slicing results. A detailed model description is provided in Duncan et al. (2007) and Strahan et al. (2007). Here, we provide a brief explanation of the model. The model is driven by Goddard Earth Observing

7

System 5 (GEOS-5) meteorological fields (Rienecker et al., 2011). The GMI spatial resolution is 2° latitude× 2.5 ° longitude. The GMI vertical extent is from the surface to 0.01 hPa, with 72 levels; vertical resolution ranges from ∼150 m in the boundary layer to ∼1 km in the free troposphere and lower stratosphere. Model outputs are sampled at the local time of the Aura overpass.

The GMI chemistry combines stratospheric chemical mechanisms (Douglass et al., 2004) with detailed tropospheric O_3-NO_x-hydrocarbon chemistry that has its origins in the Harvard GEOS-Chem model (Bey et al., 2001). In addition to chemistry, the model includes various emissions sources, aerosol microphysics, deposition, radiation, advection, and other important chemical and physical processes including lightning NO_x production (Allen et al., 2010).

In this study, we extract GMI NO_2 concentrations/burdens for four different sets of conditions and vertical ranges (three tropospheric and one stratospheric): (1) tropospheric NO_2 VMRs for heavily cloudy conditions (cloud optical thickness $\tau > 10$), (2) tropospheric NO_2 VMRs for all-sky conditions, (3) lightning contribution to the tropospheric NO_2 VMRs, and (4) stratospheric column NO_2. The contribution of lightning to tropospheric NO_2 is obtained by subtracting a no-lightning run from the full run with lightning for all-sky conditions. For comparison with OMI cloud slicing tropospheric VMRs, we average the GMI NO_2 VMRs over the appropriate OMI scene pressure range.

3   Cloud slicing technique

The cloud slicing technique takes advantage of optically thick clouds to estimate a VMR of a target trace gas in the free troposphere between the clouds (Ziemke et al., 2001, 2003). We infer NO_2 VMRs using the slope derived from linearly fitting the collocated OMI above-cloud column NO_2 to cloud scene pressures. Figure 1 illustrates a simple example of this technique (not to scale). We require at least two nearby above-cloud NO_2 VCDs for different cloud scene pressures as in Fig. 1-(a). The two OMI measurements are shown in a pressure-VCD coordinate plane in Fig. 1-(b). NO_2 VCD (VCD_{NO_2}) between the two pressure levels P1 and P2 (P1 < P2) can be derived by integrating the NO_2 VMR (VMR_{NO_2}) over pressure from P1 to P2, i.e.,

$$\mathrm{VCD_{NO_2}}_{P1}^{P2} = \frac{R_{air}}{k_B g} \times \int\limits_{P1}^{P2} \mathrm{VMR_{NO_2}}(P)\, dP, \tag{5}$$

where R_{air} is the gas constant, k_B is the Boltzmann constant, and g is the gravitational acceleration. Assuming a constant mixing ratio over the range P1 to P2 in Eq. 5, the mean NO_2 VMR in this pressure interval is given by

$$\mathrm{VMR_{NO_2}} = \frac{\Delta \mathrm{VCD}}{\Delta P} \frac{k_B g}{R_{air}}. \tag{6}$$

From this relationship, the NO_2 VMR in the pressure range of OMI cloud measurements is proportional to the fitted slope of NO_2 VCD versus cloud scene pressure, as shown in Fig. 1-(c). The

8

confidence interval of NO$_2$ VMR also can be derived from the linear fit if more than two observations are available. In Fig. 1-(c), we show the pressure range of the NO$_2$ VMR (vertical error bar) as well as the confidence interval (horizontal error bar).

In addition, a stratospheric column NO$_2$ can be derived by extrapolating the linear fit to the tropopause as shown in Fig. 1-(d). This estimate is based on the assumption that the mixing ratio of NO$_2$ remains constant from the lowest cloud pressure to the tropopause. By assuming a uniform free tropospheric NO$_2$ VMR, we limit the number of retrieved parameters to 2 (slope and y-intercept, related to free-tropospheric VMR and stratospheric VCD, respectively). This simplifies the retrieval and its error analysis.

While the cloud slicing technique derives the free tropospheric NO$_2$ VMR without the need for a prescribed stratospheric column or other a priori information, it relies on several assumptions and conditions. The method works well only with a relatively large number of nearby cloudy OMI pixels that have a sufficient variation in cloud pressure. We also note that the derived NO$_2$ VMR information is based on the assumption that NO$_2$ is vertically and horizontally well mixed in the given pressure range and spatial extent of the OMI pixel collections. In addition, we assume that the stratospheric column remains constant during the time period and over the area of the OMI pixel sample. Finally, the absolute magnitudes of the derived tropospheric mixing ratios and stratospheric columns are only as accurate as the above-cloud NO$_2$ VCDs. Errors in the derived cloud scene pressures may contribute additional uncertainty. It should also be noted that the NO$_2$ VMRs are derived in highly cloudy conditions. These conditions may not be representative of the general all-sky atmosphere.

In order to ensure that appropriate data are used for cloud-slicing, we apply rigorous data filtering criteria. This results in the use of approximately 10-15 % of the available pixel data depending on season and geolocation. The data selection criteria are summarized in Table 1 and discussed in detail in Appendix A1.

Although we show a case of two adjacent OMI measurements in Fig. 1 for simplicity, we typically use an OMI pixel collection that consists of a number of nearby measurements collected over one OMI orbit; this minimizes the effects of random errors from both the above-cloud OMI NO$_2$ VCD and P_{scene}. Examples are discussed in detail in Sect. 4.1. The detailed methodology used to obtain the seasonal climatologies is explained in Appendix A2 and Section 4.2.

4 Results and discussions

4.1 Evaluation of OMI NO$_2$ VMR with INTEX-B data

In this section, we evaluate OMI NO$_2$ VMRs derived from cloud slicing using aircraft in situ NO$_2$ measurements made during INTEX-B. For individual comparisons, we use OMI pixel collections from a single orbit that must have occurred within 2 days of an aircraft measurement. Furthermore,

9

the absolute value of the difference in the time of day between the aircraft and satellite measurements must be < 5 hours. We use relatively relaxed temporal collocation criteria (different days for OMI and INTEX-B NO_2 measurements) because most of the aircraft column measurements (from aircraft spirals) are made in clear conditions (Singh et al., 2009) while cloud slicing from OMI requires highly cloudy conditions.

To meet the spatial collocation requirements, OMI pixels must be within a box of 8° latitude × 10° longitude, centered at the location of each INTEX-B profile; we use this relatively large box to ensure the availability of an adequate number of OMI cloudy pixels. If we have multiple OMI pixel collections from adjacent days for a single aircraft profile, we average the derived VMRs from all applicable collections. Even with these relatively relaxed collocation criteria, we obtained matchups in only a few areas.

Figure 2 shows examples of cases of reasonably good agreement (within the calculated uncertainties) between OMI cloud slicing and INTEX-B NO_2 VMR. For each row, the first column shows the collection of above-cloud NO_2 columns and cloud scene pressures (light blue dots) and the fitted slope (black line) with the date of the OMI measurement, similar to Fig. 1-(b). Here, Δt refers to the aircraft minus OMI time differential. The second column, similar to Fig. 1-(c), shows the OMI cloud slicing NO_2 VMR marked by a square in the same color as used in the first column (light blue). The vertical error bar represents the applicable OMI cloud scene pressure range, and the horizontal error bar is the 95% confidence interval of the retrieved VMR.

Also shown are the collocated INTEX-B NO_2 profiles (dark blue lines) with the corresponding standard errors of the mean (gray shaded areas) and the date of the DC-8 aircraft measurement. We also show the average of the INTEX-B NO_2 VMR over the OMI cloud scene pressure range (dark blue square). The vertical and horizontal error bars represent the pressure range and the standard error of the mean for the INTEX-B measurements, respectively. This standard error of the mean (blue horizontal error bar) is smaller than that of the profiles (gray shaded area), as more VMR measurements are averaged. The third column shows the location of OMI pixels and INTEX-B profiles (in the same colors as used in the first and the second columns).

The top row of Fig. 2 shows an example of NO_2 observations over a populated area. The INTEX-B profile was measured near Houston, TX on 19 March 2006. OMI cloudy observations were made on the same day. According to the flight report, this flight segment was affected by clouds; thus this is one of the very few cases when cloudy aircraft measurements coincide with OMI cloud slicing results. The INTEX-B free tropospheric NO_2 profile is fairly uniform for P<880 hPa, while the profile shows a sharp vertical gradient for P $\gtrsim$ 900 hPa. We use only OMI pixels with $P_{scene} < 900$ hPa, thereby avoiding pixels affected by the sharp NO_2 profile gradient. The retrieved OMI VMR agrees moderately well with the INTEX-B profile for this case (OMI minus INTEX-B difference of ~17 pptv or 32 %). The high bias of the OMI NO_2 VMR is consistent with the OMI NO_2 SCD bias (25%) reported by Krotkov (2013).

305   The bottom row in Fig. 2 shows an example for a clean oceanic region, measured over the north-east Pacific on 8 May 2006. The INTEX-B profile has a significantly lower average NO_2 VMR, and the profile is nearly uniform throughout the measured pressure range. There are no surface NO_x emission sources in this region, and there is no evidence of a significant elevated NO_2 pollution plume. The OMI above-cloud column NO_2 has higher values than in the Houston case at 30° N in

310   March, presumably because the stratospheric column NO_2 is higher in this Pacific case at 45° N in May (see Fig. 7), giving a higher baseline value to the above-cloud columns. The retrieved OMI NO_2 VMR has a large confidence interval as a result of the large scatter in the above-cloud OMI NO_2 column. Nevertheless, the obtained OMI NO_2 VMR and the INTEX-B NO2 profile agree moderately well (OMI minus INTEX-B difference ∼10 pptv or 35 %), again consistent with the

315   high bias of OMI NO_2 SCDs as discussed above.

Although there are several examples of relatively good agreement as shown in Fig. 2, there are also a number of cases with significant discrepancies. There may be several reasons these differences. Firstly, the INTEX-B NO_2 profiles were obtained in relatively cloud-free conditions (except for a few cases including the 19 March 2006 profile shown in Fig. 2). Cloud conditions may alter

320   NO_x-O_3 photochemistry; this poses an intrinsic problem for the comparison. Spatial and temporal variability of tropospheric NO_2 also contribute to differences between aircraft and satellite data given the relaxed collocation criteria. We show examples of discrepancies between OMI and aircraft data in Appendix B.

Figure 3 summarizes all comparisons between OMI and INTEX-B NO_2 VMRs. We analyzed

325   all successful collocations of INTEX-B profiles and OMI cloud slicing NO_2 VMRs and produced a scatter diagram in the left panel of Fig. 3. The vertical error bars are the 95% confidence intervals of OMI NO_2 VMRs, and the horizontal error bars are the standard error of the mean of INTEX-B NO_2 VMRs. The INTEX-B standard error of the mean is small ($\lesssim$ 3 pptv) as compared with the magnitude of the NO_2 VMR, except for two cases that deviate significantly from the 1:1 line (∼6

330   pptv) marked in red color in the left panel of Fig. 3. The locations of the INTEX-B profiles are presented in the right panel of the Fig 3, with high standard error cases marked in red. The left panel using all the matchups shows significant scatter; the root mean square (RMS) of the difference is $\simeq$ 44 pptv. OMI and INTEX-B VMRs do not show any correlation. However, if we remove the INTEX-B profiles with high standard errors, OMI and INTEX-B VMRs exhibit a weak correlation

335   (R=0.3) and the scatter is reduced (RMS differences $\simeq$36 pptv). In either case, the mean OMI VMR (36–39 pptv) is larger than that of the INTEX-B VMR (22–27 pptv). These differences are in the same direction and general range (25-44%) of the suspected OMI NO_2 SCD high bias (25%). Overall, this comparison, even with its intrinsic limitations, provides some confidence in the ability to estimate NO_2 mixing ratios with OMI cloud slicing.

340   For comparison between OMCLDRR and OMCLDO2 results, a scattergram using OMI VMRs derived with OMCLDO2 cloud data is presented in Appendix D. OMCLDO2 results show similar

11

magnitudes and scatter as compared with OMCLDRR. When we exclude the high standard error cases, OMCLDO2 data result in slightly higher scatter and lower correlation versus INTEX-B.

4.2 Global Seasonal Climatology of free tropospheric NO_2 VMR

345 We construct a seasonal climatology of OMI free tropospheric NO_2 as explained in Sect. 3 and Appendix A2. In analyzing the global climatology, we focus on spatial and temporal variations of the NO_2 VMR rather than its absolute magnitude. In this section, we examine aspects of the OMI free tropospheric NO_2 climatology in the context of anthropogenic and lightning contributions. We also show GMI free tropospheric NO_2 VMRs for comparison.

350 Details regarding the construction of the climatology are provided in Appendix A2. NO_2 VMRs are not obtained where clouds rarely form (e.g., Sahara) or where cloud pressure variability is small (e.g., oceanic areas with persistent low clouds due to subsidence, such as off the western coasts of South America and southern Africa). As we sample GMI output over the OMI cloud pressure range, we do not obtain GMI NO_2 VMRs where OMI NO_2 VMRs and the corresponding cloud pressure
355 range are not reported.

Here, we note the possible sampling biases in the NO_2 climatology. Since we collect OMI measurements in cloudy scenes, the climatology represents NO_2 VMRs in highly cloudy conditions as explained in Sect. 3. In addition, because NO_2 VMRs are retrieved only if significant cloud pressure variability exists, the sampled NO_2 VMRs may be indicative of those found in presence of frontal
360 storms, where uplift of boundary layer pollution can frequently occur.

We use the standard error as an estimate of uncertainty for the derived NO_2 climatology; this assumes that the error of the derived NO_2 VMR has zero mean and that errors for individual measurements are random and uncorrelated with respect to each other. While these assumptions are not likely to strictly hold (there are indications of a bias), they may lead to reasonable uncertainties with
365 respect to the derived spatial and temporal patterns. We show the NO_2 VMR climatology where the standard error <10 pptv (if VMR <20 pptv) or 50% (if VMR >20 pptv). For more details regarding quality assurance, see Appendix C. In addition to the standard errors, we present auxiliary data to help interpret the climatology, including the number of measurements, confidence intervals, standard deviations, and the mean cloud scene pressures corresponding to the NO_2 climatology in Fig. C1 of
370 Appendix C.

Fig. 4 shows global data averaged over Jun-Aug (left column) and Dec-Feb (right column) for 2005–2007. The first row shows the OMI-derived 3-month seasonal climatology of free tropospheric NO_2 VMRs. The second row displays the GMI NO_2 VMRs in cloudy ($\tau > 10$) conditions, averaged over the corresponding OMI cloud scene pressure range. The effect of clouds on NO_x chemistry
375 is complex; it depends on altitude with respect to clouds. For example, NO_2 photolysis rates may be increased above or within bright clouds, but decreased below them. In general, the GMI cloudy VMRs are higher than those in all-sky conditions over urban regions and lower over remote and

12

oceanic regions (see Fig. C2 in Appendix C). The third row shows lightning contributions to the free tropospheric NO_2 as taken from the GMI model. Note that we use a log scale for NO_2 VMRs to highlight seasonal and spatial variations. In Appendix C, we show additional NO_2 fields for reference including GMI all-sky NO_2 VMR, OMI tropospheric column NO_2, and GMI tropospheric column NO_2.

Overall, the OMI VMR maps show some notable differences with respect to GMI, while the OMI and GMI tropospheric column maps in Appendix C look very similar. Below, we examine the potential contributions from different sources by analyzing rough vertical profiles (Sect. 4.3) as well as temporal/spatial variations of free tropospheric VMRs (Sect. 4.2.1 and 4.2.2). Further analysis related to the differences between OMI and GMI free tropospheric NO_2 is ongoing.

4.2.1 Anthropogenic contributions

In the northern hemisphere (NH) winter (Dec-Feb), the primary source of free tropospheric NO_2 appears to be anthropogenic emissions; high free tropospheric VMRs are seen over densely populated regions and the lightning contribution is expected to be negligible during these months (top right panel of Fig. 4). Over most of the highly populated areas of North America, southeast (SE) Asia, and Europe, free tropospheric NO_2 VMRs are higher in winter (Dec-Feb) as compared with summer (Jun-Aug). It is well known that boundary layer NO_2 VMRs are generally higher in winter as compared with summer owing to a longer chemical lifetime in winter; the OMI-derived tropospheric columns (the first row of Fig. C3 in Appendix C), that are dominated by boundary layer pollution in heavily populated areas, also reflect higher values in winter than in summer. In contrast to NO_2 VMRs from OMI, the NO_2 VMRs from GMI are higher in summer as compared with winter over southeast Asia (the second row of Fig. 4 for cloudy conditions, and Fig. C2 for all-sky conditions), while the tropospheric column NO_2 from GMI is higher in winter in this region (the second row of Fig. C3 in Appendix C). Examination of GMI NO_2 and NO vertical profiles confirms that this is not a simple partitioning problem of NO_x.

Overall, OMI NO_2 VMRs have lower values in the SH during the austral winter as compared with the NH. This is also shown in the GMI output. It should be noted that there are not many large population centers in the SH, particularly at high latitudes, nor as much NO_x contribution from aircraft at high latitudes in the SH as compared with the NH. However, it should also be noted that cloud slicing data are not available around many of the major population centers in the SH (e.g., Johannesburg, South Africa and Sao Paulo, Brazil) owing to a lack of optically thick clouds and/or cloud pressure variation.

Regarding transport of anthropogenic NO_2, we focus on winter months when lightning NO_2 contributions are likely to be small. The OMI cloud slicing NO_2 climatology shows a spatial patterns consistent with pollution outflow from North America and Asia. For example, the persistent Asian northeasterly outflow of NO_2 via the Bering Sea resembles that of CO (e.g., Liang et al., 2004), a

13

tracer of incomplete combustion emissions. The spatial extents of continental outflows are different for the free tropospheric VMRs and tropospheric columns. This might be explained by extended transport at higher altitudes where the NO_2 lifetime is longer.

4.2.2 Lightning contributions

A band of enhanced NO_2 appears extensively during the summer in the both hemispheres ($\sim$0–30° and possibly higher latitudes in the NH). The low cloud scene pressures (shown in the fifth row of Fig. C1 in Appendix C) in these regions are indicative of frequent convection. In particular, extensive enhancements in summertime NO_2 VMRs over NH tropical and subtropical oceans, are similar to modeled lightning NO_x enhancements in previous studies (e.g., Choi et al., 2008; Allen et al., 2012; Martini et al., 2011; Walker et al., 2010). This suggests that lightning is a major source of free tropospheric NO_2 in tropical and subtropical regions in summer. Because the SH is far less polluted than the NH, potential NO_2 enhancements due to lightning are more apparent there. Finally, we note that these extensive NO_2 enhancements indicated by cloud slicing during summer over oceans are not as apparent in the OMI tropospheric columns.

While the locations of these apparent lightning-enhancements of NO_2 are similar in summer in both GMI and OMI data sets, there are a few key differences to note. For example, the seasonality of the NO_2 enhancements over oceans shown by OMI is not as strongly reflected in the GMI output. In addition, there appears to be a much stronger land/ocean contrast in GMI than in the OMI climatology.

For comparison, we also show maps of free-tropospheric NO_2 climatology obtained with OMCLDO2 cloud data in Fig. D2 of Appendix D. The OMCLDO2 climatology shows very similar spatial and temporal patterns as compared with that derived using OMCLDRR data presented here with slightly lower VMRs in general. However, the OMCLDO2 climatology does not show a strong signature of lightning-enhanced NO_2 over the tropical North Pacific in Jun-Aug as is shown in the OMCLDRR climatology. This is discussed in more detail in Appendix D.

4.3 Profile analysis

We examine the pressure dependence of the derived VMRs over large regions (to reduce random errors) in order to provide a rough vertical distribution of free tropospheric NO_2. We highlight two types of areas: (1) East Asia and its outflow region to focus on anthropogenic contributions, and (2) tropical portions of the NH and SH to examine potential lightning contributions.

Figure 5 shows NO_2 profiles obtained over East Asia and its outflow region in summer 2005–2007; in this region and season, a large number of cloudy pixels are available and cloud pressures exhibit enough variability to construct profiles due to the large sampling area and monsoon. This is not the case for many other urban regions and seasons. The sampling areas are shown in blue (East Asia) and purple (outflow) on the maps, and the corresponding profiles are presented in the same

14

colors. The standard errors are also shown and are relatively small owing to the large number of
450   samples. We note that NO_2 profile information is not obtained in the lowermost troposphere over
East Asia; we attempt to avoid boundary layer contamination in order to preserve the assumption
of uniform NO_2 VMRs over the observed cloud pressure range. We obtain a profile down to 850
hPa in the outflow region because there is little boundary layer pollution in that area.The profile of
East Asia clearly indicates the presence of uplifted anthropogenic NO_2 in the middle troposphere of
455   600-800 hPa. In the outflow region, the NO_2 VMRs are higher at P$\lesssim$700 hPa as compared with those
at P$>$ 800 hPa. This suggests that there is not a significant surface source NO_2, and that uplifted
anthropogenic NO_2 is transported at around $\sim$700 hPa or above in this region.

Figure 6 shows variations in the derived NO_2 profiles in tropical regions of the NH and SH. Here,
we examine two latitudinal bands with enhanced summertime NO_2 based on the spatial distributions
460   shown in Fig. 4. Again, owing to the large number of samples, the standard errors are relatively small
($\sim$5 pptv). In summer, the NO_2 VMRs increase with altitude in both hemispheres. The profile shapes
suggest that NO_2 sources, presumably lightning, are located primarily in the upper troposphere
in these regions. This is consistent with aircraft measurements (e.g., Huntrieser et al., 2009) and
modeling studies (e.g., Allen et al., 2010, 2012; Martini et al., 2011) of lightning-generated NO_x. In
465   contrast, NO_2 VMR profiles are more uniform in winter, possibly owing to less frequent lightning
activity associated with convection in the shifting Inter-Tropical Convergence Zone (ITCZ). We note
that the winter baseline NO_2 VMR is higher in NH by approximately a factor of two possibly due to
more pollution sources in NH. In contrast, the summertime profiles of NO_2 are very similar in the
NH and SH.

470   Overall, our analysis indicates a capability of the cloud slicing technique to retrieve NO_2 profile
information when provided with a relatively large sample size. Our profile results are consistent with
an anthropogenic source for the enhanced NO_2 in middle to high latitudes off the coasts of highly
populated areas. They also indicate a lightning source in the summer over tropical areas, primarily
located in the upper troposphere.

475   ## 4.4   Stratospheric column NO_2

We generated estimates of stratospheric NO_2 columns as described in Sect. 3. As done for the
free tropospheric NO_2 VMRs, the derived stratospheric columns of NO_2 are averaged for 3 month
intervals using data collected from 2005–2007. Zonal means are shown as a function of latitude in
Fig. 7. We also show the estimates of stratospheric NO_2 columns from OMNO2B (derived using a
480   completely different method as discussed in Sect. 2.1.3) and GMI. Both the OMI cloud slicing and
OMNO2B stratospheric NO_2 column estimates show similar zonal structure as compared with that
from GMI in all seasons. Note that both OMI estimates are $\sim$30% higher than GMI; this is consistent
with the expected high bias described in Sect 2.1.2. The overall excellent agreement between the
cloud-slicing stratospheric column and other independent estimates provides a closure check on the

485 derived free tropospheric NO_2 VMRs; if the cloud-slicing procedure was not performing well in the free troposphere, we would not obtain reasonable stratospheric column estimates. Therefore, this exercise provides validation of both stratospheric and free tropospheric results. Estimates of stratospheric columns from OMCLDO2 product display similar zonal structure as compared with those from OMCLDRR (not shown).

5 Conclusions

We have estimated free tropospheric NO_2 VMRs and stratospheric NO_2 columns using a cloud slicing approach applied to OMI data from 2005 to 2007. Optically thick clouds provide excellent sensitivity of satellite radiances to NO_2 above the cloud scene pressure; they also effectively shield satellite observations from NO_2 below clouds. In order to retrieve NO_2 VMRs, our approach requires 495 a large number of cloudy measurements with substantial cloud pressure variability.

We conducted a detailed comparison between OMI cloud slicing free tropospheric NO_2 VMRs and INTEX-B aircraft in situ measurements. Our analysis shows that the cloud slicing technique provides similar magnitudes as compared with in situ measurements when known satellite biases are taken into consideration. However, individual comparisons of INTEX-B and cloud slicing NO_2 500 VMRs do not always exhibit good agreement. Small-scale temporal and spatial variability, poor collocation, and fairly large OMI measurement uncertainties contribute to these discrepancies.

We generated global seasonal maps of free tropospheric NO_2 VMRs as well as free tropospheric NO_2 vertical profiles over selected regions. With appropriate data filtering over a three year time period, we obtain a sufficient number of cloudy OMI measurements to cover most of the Earth. 505 Confidence intervals for individual cloud slicing VMRs are fairly large; however, averaging over nine months (3 months $\times$ 3 years) reduces random errors and provides a reasonable estimate of the mean values. The free-tropospheric NO_2 VMR climatology shows distinct spatial and seasonal patterns; these patterns differ from those of OMI-estimated tropospheric NO_2 columns. The combination of mapped and profile analyses indicates that spatial patterns of the OMI-derived free tropospheric NO_2 510 are consistent with (1) uplifted anthropogenic NO_2 over densely populated regions; (2) continental outflow of anthropogenic NO_2; and (3) lightning-generated NO_x, particularly in summer months at low to middle latitudes with a source located primarily in the upper troposphere. Anthropogenic sources appear to dominate in the winter hemisphere, especially in the northern hemisphere at high latitudes near heavily populated regions, while lightning contributions dominate over ocean at low 515 to middle latitudes in summer in both hemispheres.

GMI model simulations suggest that NO_2 VMRs vary with cloud conditions by altering the photochemistry. Spatial patterns of continental outflow show general agreement between the OMI cloud slicing climatology and GMI simulations for cloudy conditions. However, some differences, particularly with respect to lightning-generated NO_x, were noted.

16

520   We also provided estimates of NO_2 stratospheric columns from the cloud slicing technique. These
estimates agree well with those from the OMNO2B algorithm that are based on a completely inde-
pendent technique (NO_2 columns over clean regions). The two OMI stratospheric NO_2 estimates
display similar seasonal and latitudinal zonal mean variations. These variations are also consistent
with those produced in GMI simulations. The excellent agreement between these stratospheric col-
525   umn NO_2 estimates provides a closure validation of the free tropospheric OMI cloud slicing results.

Our overall analysis shows that the cloud slicing technique can provide valuable information on
the free tropospheric distribution of NO_2 that is distinct from the derived tropospheric total columns.
In particular, we expect to apply this technique to future geostationary missions including the NASA
Earth Ventures Instrument (EVI) 1 selected mission Tropospheric Emissions: Monitoring of Pollu-
530   tion (TEMPO) over the North America (Chance et al., 2013) and the Korean Geostationary Environ-
ment Monitoring Spectrometer (GEMS) over the Asia-Pacific region (Kim, 2012). These missions
should provide excellent cloud slicing results; they will provide improved sampling (with higher
spatial and temporal resolutions) as compared with OMI.

Appendix A

535   **Additional details in applying the cloud slicing technique**

A1   Data Filtering Criteria

We apply the following checks to ensure that only high quality data are used in our analysis. With
these checks, approximately 10-15 % of OMI pixels are retained, depending on season and geoloca-
tion: (1) we use only pixels with $f_r > 0.9$ to remove OMI pixels with an insufficient cloud shielding
540   of the boundary layer; (2) we remove data with aerosol indices > 1.0, because absorbing aerosols are
known to produce biases in the retrieved cloud properties (Vasilkov et al., 2008); (3) we exclude data
with solar zenith angles (SZA) $> 80°$; the use of the geometrical AMFs may not be appropriate at
higher SZAs owing to higher amounts of Rayleigh scattering; (4) we exclude data affected by snow
and ice because UV/VIS cloud measurements cannot differentiate between snow/ice and clouds; In
545   the presence of snow/ice, we cannot be assured of boundary layer cloud shielding. We use a flag
for snow- and ice-covered pixels based on the Near-real-time SSM/I EASE-grid daily global Ice and
snow concentration and Snow Extent (NISE) data set (Nolin et al., 1998) provided in OMCLDRR
product.

We also apply checks to ensure sufficient cloud variability; we only use collections with at least
550   30 OMI pixels, a cloud pressure standard deviation > 35 hPa, and a cloud pressure range > 200
hPa. Finally, we employ outlier checks to remove data that fall outside the range expected from our
assumptions including a uniform mixing ratio over the appropriate pressure range and homogeneous
stratospheric column over the corresponding area; we empirically selected a threshold of 2σ from

the linear fit for this check.

A2   Application of cloud slicing to seasonal climatology

In order to create a global seasonal climatology of free-tropospheric NO_2 VMRs, we average individual retrievals in three month segments (one for each season) using data collected over 3 years (2005–2007). We grid the data at a spatial resolution of 6° latitude × 8° longitude.

In Fig. A1, we show two examples of how the NO_2 VMRs are calculated for a single grid box. For these examples, we use only one month in summer (June) and winter (January). The grid box encompasses New York City, NY, USA. In order to remove pixels affected by substantial vertical gradients in the NO_2 VMR, we use only cloudy data with P_{scene} < a lower boundary (P_{lower}, gray lines) where the mean NO_2 vertical profile is relatively well mixed according GMI; specifically, P_{lower} is pressure above which the absolute magnitude of vertical gradient of monthly-mean NO_2 VMR < 0.33 pptv/hPa. Note that P_{lower} varies with season (as shown in Fig. A1) and geolocation (not shown). For reference, we also show GMI daily and monthly mean profiles.

Using an OMI pixel collection from a single orbit, we calculate the free tropospheric NO_2 VMR (small black dots), the confidence interval (horizontal bars), and the pressure range (vertical bars). Then, we average the derived single-orbit NO_2 VMRs (weighted inversely by the square of the confidence intervals) to obtain a single representative NO_2 VMR for the given time period (large black dots).

In Fig. A1, we have shown data from one month for simplicity. To construct a seasonal climatology, we use the same spatial grid but a larger temporal window (3 months×3 years) to reduce the sampling biases and random noise. For quality control of the climatology, we show data only where the NO_2 VMR standard error of the mean < 50% for NO_2 VMR > 20 pptv or NO_2 VMR standard error of the mean < 10 pptv for NO_2 VMR ≤ 20 pptv. With these criteria, there are some areas with no OMI-derived NO_2 VMRs. These are mainly areas with little variability in cloud pressure or regions covered with ice/snow. A similar approach is used to obtain gridded values of the stratospheric NO_2 column.

Appendix B

Additional case studies of OMI and INTEX-B comparisons

We show additional comparisons in which OMI and INTEX-B NO_2 VMR display poor agreement. These discrepancies are presumably caused by small-scale spatial and temporal variations in NO_2 VMRs, different cloud conditions that might alter the NO_x photochemistry, and/or poor collocations.

Figure B1 shows a case with discrepancies likely due to the differences in the locations, times, and the spatial scales of the measurements. The DC-8 profile was taken over a small area near Houston

18

in the morning ($\sim$8:35 am LT), while the OMI pixel collection covers a large area over Louisiana in the afternoon ($\sim$1:35 pm LT) on the same day; thus the OMI and DC-8 measurements were taken in adjacent locations with a $\sim$5 hour time gap. The DC-8 NO_2 profile (second column) appears to be affected by local pollution in the 600-800 hPa range. In contrast, OMI retrieves a low NO_2 VMR over a wide area that includes less populated regions. OMI and INTEX-B VMRs show a significant difference of $\sim$50pptv in this case.

Figure B2 shows an example of small scale spatial variations in NO_2 profiles as seen by the aircraft measurements. The second column of Fig. B2 shows two DC-8 NO_2 profiles that were taken on the same day at nearby locations. The first column shows the two corresponding OMI pixel collections closest to the DC-8 profiles. In order to differentiate the two cases, the first row uses dark blue for tne DC-8 profile and light blue for OMI pixels, and the second row uses red for the DC-8 profile and pink for OMI pixels. Since the two DC-8 profiles encompass many of the same OMI pixels, the shared pixels are marked with purple on the map (top right). Although the two DC-8 profiles are within a close proximity in both time and space, the averaged NO_2 VMRs differ by about 20 pptv, perhaps due to a transported pollution plume. However, since the OMI pixel collections corresponding the two DC-8 profiles share many OMI pixels, this gives similar NO_2 OMI VMRs for the two corresponding DC-8 profiles. As a result, OMI and INTEX-B profiles differ by $\sim$30 pptv in the first row case, while the difference is smaller in the second row case, about $\sim$15 pptv.

Variability of OMI NO_2 VMRs can also cause discrepancies between OMI and INTEX-B VMRs. This variability may be due to actual variability in the NO_2 profile over the course of a day and/or errors in the OMI measurements. Figure B3 shows a case of OMI cloud slicing VMR variation between orbits for one DC-8 NO_2 profile. The first and second panels of Fig. B3 show two OMI pixel collections taken from two adjacent orbits on the same day. They correspond to one DC-8 profile taken over the Pacific north of Hawaii. Even though the OMI pixel collections cover a similar area and time, the resulting NO_2 VMRs differ by $\sim$30 pptv. This variability may be due to a small scale feature such as a transported pollution plume, altered photochemistry due to the different solar illuminations or cloud conditions, and/or measurement uncertainties in the OMI data, although the differences appear to be outside the expected OMI uncertainties.

Appendix C

Auxiliary data to interpret cloud slicing NO2 VMR

Here, we show auxiliary data that is helpful for quality assurance and interpretation of the NO_2 VMR climatology. The first row of Fig. C1 shows the gridded numbers of OMI pixel collections that are used to derive the seasonal free tropospheric NO_2 climatology. The maps show a sufficiently large

number of collections (> 60) for many areas of interest. Large numbers of collections are available over the frontal storm track regions of the North Atlantic, North Pacific and Southern ocean as well as the intertropical convergence zone (ITCZ). In addition, there are large numbers of orbits at high latitudes ($> 60°$), because these regions can have more than one overpass (orbit) per day. However, some relatively cloud free areas (e.g., the Sahara) as well as oceanic regions, in areas of subsidence with little cloud pressure variability, have smaller numbers of collections (<20).

The second row of Fig. C1 shows the weighted root mean square (RMS) of 95% confidence intervals of NO_2 VMRs. As discussed above, the confidence interval is a measure of the fitting uncertainty for single NO_2 VMRs derived from individual pixel collections, i.e. a large RMS of the confidence interval means a large uncertainty in the individually fitted NO_2 VMRs. There are two types of regions that have large uncertainties: (1) Regions with low numbers of OMI orbits, i.e, small amounts clouds or low cloud pressure variability; (2) Areas where NO_2 VMRs are high, e.g., major metropolitan areas. In these regions, we may expect larger variability in the NO_2 VCDs within a single collection.

The third row of Fig. C1 shows maps of standard deviations of the gridded climatological NO_2 VMRs. This is a measure of how much the individually fitted NO_2 VMRs vary in each grid box. Similar to the confidence interval, the standard deviations are large in areas of high NO_2 VMRs (major urban areas and continental plumes) and areas with small clouds amounts and/or small cloud variability (deserts and oceans near 20°N latitude). In addition, high standard deviations are present near $\sim$60°S in Sep.-Nov., possibly owing to stratospheric variability and/or larger errors at high solar zenith angles.

The fourth row of Fig. C1 shows maps of the standard error of the mean for the gridded NO_2 VMR climatology (i.e., the standard deviation divided by square root of the number of measurements). The standard errors provide an estimate of uncertainty for the spatial and temporal variations shown in the climatology (in the absence of a constant bias). We use this quantity for quality control as described in Sect. 4.2.

The fifth row of Fig. C1 shows maps of the OMCLDRR cloud scene pressure for the gridded NO_2 VMR climatology. Owing to significant light penetration inside clouds, the lowest mean cloud pressures are around 450 hPa, well below the typical cloud top pressures. The cloud pressures also vary with season.

Figure C2 shows seasonal mean GMI free tropospheric NO_2 VMRs for all-sky conditions. While the maps of all-sky VMR show similar patterns as compared with those of cloudy conditions, all-sky NO_2 VMRs are generally lower over urban regions and higher over oceans than cloudy NO_2 VMRs.

Figure C3 shows tropospheric column NO_2 from OMI (upper row) and GMI (bottom row). OMI and GMI tropospheric columns NO_2 agree very well, showing higher columns in winter and lower columns in summer over major urban areas. This seasonal variation is also shown in the OMI climatology of free tropospheric NO_2 VMR as presented in Sect. 4.2.1.

20

Appendix D

OMCLDO2 sample results

660 While we used OMCLDRR cloud parameters for analysis in the main text, here we show results obtained when using cloud parameters from the OMCLDO2 product. Similar to Fig. 3, Figure D1 shows a scattergram of INTEX-B and OMI cloud slicing NO_2 VMRs, but using OMCLDO2 cloud data. As above for OMCLDRR, the left panel shows results from all available matchups between INTEX-B and OMI, and the middle panel shows matchups where the standard error of the mean

665 of INTEX-B measurement < 5 pptv. We note that the number of matchups is different for the OMCLDRR and OMCLDO2 results. Since OMCLDRR and OMCLDO2 report slightly different cloud scene pressures for the same OMI pixel, differences in the cloud data results in different quality control decisions, and this produces the different numbers of successful collocations. Similarly, the reported INTEX-B VMRs used in the scattergram can change with the cloud pressure data set as the

670 INTEX-B VMRs are sampled over the appropriate range of OMI-derived cloud pressures.

The RMS differences between INTEX-B and OMI NO_2 VMRs using both cloud products are similar in magnitude. OMCLDO2 results have a slightly lower correlation with INTEX-B if we exclude INTEX-B measurement with large standard errors (> 5 pptv).

Similar to the two upper rows of Fig. 4, Figure D2 shows global maps of the free tropospheric NO_2

675 climatology obtained with OMCLDO2 cloud parameters. OMCLDO2 NO_2 VMRs (first row) overall have slightly lower magnitudes as compared with OMCLDRR results. The spatial and temporal patterns of OMCLDO2 NO_2 VMR over densely populated regions as well as the continental outflow patterns are similar to those from OMCLDRR. NO_2 VMRs in areas that are thought be affected by lightning, however, display some differences. In OMCLDRR results, lightning-generated NO_2

680 appears to be present extensively during summer in the both hemispheres. In OMCLDO2 results, we can see an indication of lightning-generated NO_2 in the SH in Dec.–Feb. While we see possible lightning NO_2 signatures with OMCLDO2 over the Gulf of Mexico, the north equatorial Atlantic, and India, there is not a significant lightning NO_2 feature in the low latitudes of the NH Pacific in Jun.–Aug. as was shown in OMCLDRR results. The reasons for these differences are not well

685 understood. Joiner et al. (2010) showed that there is a high frequency of multi-layer clouds in the NH Pacific. The two cloud algorithms may behave differently in these complex conditions as Raman scattering has a linear response with cloud pressure, while oxygen dimer absorption has a pressure-squared dependence.

695 References

Acarreta, J. R., De Haan, J. F. and Stammes, P.: Cloud pressure retrieval using the O_2 -O_2 absorption band at 477 nm, J. Geophys. Res., 109(D5), D05204, doi:10.1029/2003JD003915, 2004.

Ahmad, Z., Bhartia, P.K. and Krotkov, N.: Spectral properties of backscattered UV radiation in cloudy atmospheres. J. Geophys. Res., 109, 0148–0227, doi:10.1029/2003JD003395, 2004.

700 Allen, D., Pickering, K., Duncan, B. and Damon, M.: Impact of lightning NO emissions on North American photochemistry as determined using the Global Modeling Initiative (GMI) model, J. Geophys. Res., 115(D22), D22301, doi:10.1029/2010JD014062, 2010.

Allen, D. J., Pickering, K. E., Pinder, R. W., Henderson, B. H., Appel, K. W. and Prados, A.: Impact of lightning-NO on eastern United States photochemistry during the summer of 2006 as determined using the 705 CMAQ model, Atmos. Chem. Phys., 12(4), 1737–1758, doi:10.5194/acp-12-1737-2012, 2012.

Beirle, S., Platt, U., von Glasow, R., Wenig, M., and Wagner, T.: Estimate of nitrogen oxide emissions from shipping by satellite remote sensing, Geophys. Res. Lett., 31, L18102, doi:10.1029/2004GL020312, 2004.

Beirle, S., Boersma, K. F., Platt, U., Lawrence, M. G., and Wagner, T.: Megacity Emissions and Lifetimes of Nitrogen Oxides Probed from Space, Science, 333, 1737–1739, 2011.

710 Bey, I., Jacob, D. J., Yantosca, R. M., Logan, J. A., Field, B. D., Fiore, A. M., Li, Q., Liu, H., Mickley, L. J., and Schultz, M. G.: Global modeling of tropospheric chemistry with assimilated meteorology: Model description and evaluation, J. Geophys. Res., 106, 23073–23095, 2001

Boersma, K. F., Eskes, H. J., Meijer, E. W. and Kelder, H. M.: Estimates of lightning NOx production from GOME satellite observations, Atmos. Chem. Phys., 5(9), 2311–2331, 2005.

715 Boersma, K. F., Eskes, H. J., Veefkind, J. P., Brinksma, E. J., van der, R. J., Sneep, A. M., van den Oord, G. H. J., Levelt, P. F., Stammes, P., Gleason, J. F., and Bucsela, E. J.: Near-real time retrieval of tropospheric NO2 from OMI, Atm. Chem. Phys., 2013–2128, doi:10.5194/acp-7-2103-2007, 2007.

Boersma, K. F., Jacob, D. J., Bucsela, E. J., Perring, A. E., Dirksen, R., van der A, R. J., Yantosca, R. M., Park, R. J., Wenig, M. O. and Bertram, T. H.: Validation of OMI tropospheric NO_2 observations during INTEX-B 720 and application to constrain NOx emissions over the eastern United States and Mexico, Atmos. Environ., 42(19), 4480–4497, doi:10.1016/j.atmosenv.2008.02.004, 2008.

Boersma, K. F., Eskes, H. J., Dirksen, R. J., van der A, R. J., Veefkind, J. P., Stammes, P., Huijnen, V., Kleipool, Q. L., Sneep, M., Claas, J., Leitão, J., Richter, A., Zhou, Y. and Brunner, D.: An improved tropospheric NO_2 column retrieval algorithm for the Ozone Monitoring Instrument, Atmos. Meas. Tech., 4(9), 1905–1928, 725 doi:10.5194/amt-4-1905-2011, 2011.

Bovensmann, H., Burrows, J. P., Buchwitz, M., Frerick, J., Noël, S., Rozanov, V. V., Chance, K. V., and Goede, A. P. H.: SCIAMACHY: Mission Objectives and Measurement Modes, J. Atmos. Sci., 56, 127–150, 1999.

Bowman, K. and Henze, D. K.: Attribution of direct ozone radiative forcing to spatially resolved emissions, Geophys. Res. Lett., 39(22), L22074, doi:10.1029/2012GL053274, 2012.

730 Brook, J. R.; Burnett, R. T.; Dann, T. F.; Cakmak, S.; Goldberg, M. S.; Fan, X.; Wheeler, A. J.Further interpretation of the acute effect of nitrogen dioxide observed in Canadian time series studies, J. Exposure Sci. Environ. Epidemiol., 17, S36–S44, 2007.

Bucsela, E. J., Celarier, E. A., Wenig, M. O., Gleason, J. F., Veefkind, J. P., Boersma, K. F. and Brinksma, E. J.: Algorithm for NO_2 vertical column retrieval from the ozone monitoring instrument, IEEE Trans. Geo.

23

735   Remote Sens., 44(5), 1245–1258, doi:10.1109/TGRS.2005.863715, 2006.

Bucsela, E. J., Perring, A. E., Cohen, R. C., Boersma, K. F., Celarier, E. A., Gleason, J. F., Wenig, M. O., Bertram, T. H., Wooldridge, P. J., Dirksen, R. and Veefkind, J. P.: Comparison of tropospheric NO_2 from in situ aircraft measurements with near-real-time and standard product data from OMI, J. Geophys. Res., 113(D16), D16S31, doi:10.1029/2007JD008838, 2008.

740   Bucsela, E. J., Krotkov, N. A., Celarier, E. A., Lamsal, L. N., Swartz, W. H., Bhartia, P. K., Boersma, K. F., Veefkind, J. P., Gleason, J. F. and Pickering, K. E.: A new stratospheric and tropospheric NO_2; retrieval algorithm for nadir-viewing satellite instruments: applications to OMI, Atmos. Meas. Tech. Discuss., 6(1), 1361–1407, doi:10.5194/amtd-6-1361-2013, 2013.

Castellanos, P. and Boersma, K. F.: Reductions in nitrogen oxides over Europe driven by environmental policy
745   and economic recession, Sci. Rep., 2, 265, doi:10.1038/srep00265, 2012.

Celarier, E. A., Brinksma, E. J., Gleason, J. F., Veefkind, J. P., Cede, A., Herman, J. R., Ionov, D., Goutail, F., Pommereau, J.-P., Lambert, J.-C., van Roozendael, M., Pinardi, G., Wittrock, F., Schönhardt, A., Richter, A., Ibrahim, O. W., Wagner, T., Bojkov, B., Mount, G., Spinei, E., Chen, C. M., Pongetti, T. J., Sander, S. P., Bucsela, E. J., Wenig, M. O., Swart, D. P. J., Volten, H., Kroon, M. and Levelt, P. F.: Validation of Ozone Monitor-
750   ing Instrument nitrogen dioxide columns, J. Geophys. Res., 113(D15), D15S15, doi:10.1029/2007JD008908, 2008.

Chance, K., Liu, X., Suleiman, R. M., Flittner, D. E., Al-Saadi, J., and Janz, S. J.: Tropospheric emissions: Monitoring of pollution (TEMPO), Proc. SPIE, Vol. 8866, Earth Observing Systems XVIII, Paper 88660D, doi:10.1117/12.2024479, 2013.

755   Chandra, S., Ziemke, J. R., Duncan, B. N., Diehl, T. L., Livesey, N. J. and Froidevaux, L.: Effects of the 2006 El Niño on tropospheric ozone and carbon monoxide: Implications for dynamics and biomass burning, Atmos. Chem. Phys., 9(13), 4239–4249, 2009.

Choi, Y., Wang, Y., Zeng, T., Martin, R. V., Kurosu, T. P., and Chance, K.: Evidence of lightning NOx and convective transport of pollutants in satellite observations over North America, Geophys. Res. Lett., 32(2),
760   L02805, doi:10.1029/2004GL021436, 2005.

Choi, Y., Wang, Y., Zeng, T., Cunnold, D., Yang, E.-S., Martin, R., Chance, K., Thouret, V. and Edgerton, E.: Springtime transitions of NO_2 , CO, and O_3 over North America: Model evaluation and analysis, J. Geophys. Res., 113(D20), D20311, doi:10.1029/2007JD009632, 2008b.

Douglass A. R., Stolarski, R. S., Strahan, S. E., and Connell, P. S.: Radicals and reservoirs in the
765   GMI chemistry and transport model: Comparison to measurements, J. Geophys. Res.,109, D16302, doi:10.1029/2004JD004632, 2004.

Duncan, B. N., Strahan, S. E., Yoshida, Y., Steenrod, S. D. and Livesey, N.: Model study of the cross-tropopause transport of biomass burning pollution, Atmos. Chem. Phys., 7(14), 3713–3736, 2007.

Duncan, B. N., Yoshida, Y., de Foy, B., Lamsal, L. N., Streets, D. G., Lu, Z., Pickering, K. E. and
770   Krotkov, N. A.: The observed response of Ozone Monitoring Instrument (OMI) NO_2 columns to NO_x emission controls on power plants in the United States: 2005–2011, Atmos. Environ., 81, 102–111, doi:10.1016/j.atmosenv.2013.08.068, 2013.

Frost, G. J., McKeen, S. A., Trainer, M., Ryerson, T. B., Neuman, J. A., Roberts, J. M., Swanson, A., Holloway, J. S., Sueper, D. T., Fortin, T., Parrish, D. D., Fehsenfeld, F. C., Flocke, F., Peckham, S. E.,

775 Grell, G. A., Kowal, D., Cartwright, J., Auerbach, N., and Habermann, T.:Effecs of changing power plant NOx emissions on ozone in the eastern United States: Proof of concept, J. Geophys. Res., 111, D12306, doi:10.1029/2005JD006354, 2006.

Fuglestvedt, J., Berntsen, T., Myhre, G., Rypdal, K. and Skeie, R. B.: Climate forcing from the transport sectors, Proc. Natl. Acad. Sci. U. S. A., 105(2), 454–458, 2008.

780 Herman, J., Cede, A., Spinei, E., Mount, G., Tzortziou, M. and Abuhassan, N.: NO_2 column amounts from ground-based Pandora and MFDOAS spectrometers using the direct-sun DOAS technique: Intercomparisons and application to OMI validation, J. Geophys. Res., 114(D13), D13307, doi:10.1029/2009JD011848, 2009.

Hains, J. C., Boersma, K. F., Kroon, M., Dirksen, R. J., Cohen, R. C., Perring, A. E., Bucsela, E., Volten, H., Swart, D. P. J., Richter, A., Wittrock, F., Schoenhardt, A., Wagner, T., Ibrahim, O. W., van Roozendael, M.,
785 Pinardi, G., Gleason, J. F., Veefkind, J. P. and Levelt, P.: Testing and improving OMI DOMINO tropospheric NO 2 using observations from the DANDELIONS and INTEX-B validation campaigns, J. Geophys. Res., 115(D5), doi:10.1029/2009JD012399, 2010.

Huntrieser, H., Schlager, H., Lichtenstern, M., Roiger, A., Stock, P., Minikin, A., Höller, H., Schmidt, K., Betz, H.-D. and Allen, G.: NO_x production by lightning in Hector: first airborne measurements during SCOUT-
790 O3/ACTIVE, Atmos. Chem. Phys., 9(21), 8377–8412, 2009.

Jaeglé, L., Steinberger, L., Martin, R. V., and Chance, K.: Global partitioning of NO_x sources using satellite observations: Relative roles of fossil fuel combustion, biomass burning and soil emissions, Faraday Discuss., 130, 407–423, doi:10.1039/b502128f, 2005.

Joiner, J., and Vasilkov, A. P.: First results from the OMI Rotational Raman Scattering Cloud Pressure Algo-
795 rithm, IEEE Trans. Geosci. Rem. Sens., 44, 1272-1282, 2006.

Joiner, J., Schoeberl, M. R., Vasilkov, A. P., Oreopoulos, L., Platnick, S., Livesey, N. J. and Levelt, P. F.: Accurate satellite-derived estimates of the tropospheric ozone impact on the global radiation budget, Atmos. Chem. Phys., 9(13), 4447–4465, doi:10.5194/acp-9-4447-2009, 2009.

Joiner, J., Vasilkov, A. P., Bhartia, P. K., Wind, G., Platnick, S. and Menzel, W. P.: Detection of multi-layer and
800 vertically-extended clouds using A-train sensors, Atmos. Meas. Tech., 3(1), 233–247, 2010.

Joiner, J., Vasilkov, A. P., Gupta, P., Bhartia, P. K., Veefkind, P., Sneep, M., de Haan, J., Polonsky, I. and Spurr, R.: Fast simulators for satellite cloud optical centroid pressure retrievals; evaluation of OMI cloud retrievals, Atmos. Meas. Tech., 5(3), 529–545, doi:10.5194/amt-5-529-2012, 2012.

Kim, J.: GEMS (Geostationary Environment Monitoring Spectrometer) onboard the GeoKOMPSAT to Monitor
805 Air Quality in high Temporal and Spatial Resolution over Asia-Pacific Region, EGU General Assembly 2012, Vienna, Austria, 2012

Koelemeijer, R. B. A. and Stammes, P.: Effects of clouds on ozone column retrieval from GOME UV measurements, J. Geophys. Res., 104(D7), 8281–8294, doi:10.1029/1999JD900012, 1999.

Krotkov, N. A.: Improved OMI NO2 standard product: algorithm, evaluation, and results, the Aura Science
810 Team Meeting, Pasadena, CA, 2013.

Lamsal, L. N., Martin, R. V., van Donkelaar, A., Celarier, E. A., Bucsela, E. J., Boersma, K. F., Dirksen, R., Luo, C., and Wang, Y.: Indirect validation of tropospheric nitrogen dioxide 30 retrieved from the OMI satellite instrument: Insight into the seasonal variation of nitrogen oxides at northern midlatitudes, J. Geophys. Res., 115, D05302, doi:10.1029/2009JD013351, 2010.

815 Lamsal, L. N., Martin, R. V., Parrish, D. D., Krotkov. N. A.: Scaling Relationship for NO2Pollution and Urban Population Size: A Satellite Perspective, Env. Sci. Technol., 47(14), 7855, doi:10.1021/es400744g, 2013.

Levelt, P. F., van den Oord, G. H. J., Dobber, M.R., Mälkki, A., Visser, H., de Vries, J., Stammes, P., Lundell, J., and Saari, H.: The Ozone Monitoring Instrument, IEEE Trans. Geo. Rem. Sens., 2006, Vol. 44, No. 5, 1093–1101, doi:10.1109/TGRS.2006.872333.

820 Li, Q., Jacob. D. J., Park, R., Wang, Y., Heald, C. L., Hudman, R., and Yantosca, R. M.: North American pollution outflow and the trapping of convectively lifted pollution by upper-level anticyclone, J. Geophys. Res., 110(D10), D10301, doi:10.1029/2004JD005039, 2005.

Liang, Q., Jaeglé, L., Jaffe, D. A., Weiss-Penzias, P., Heckman, A., and Snow, J. A.: Long-range transport of Asian pollution to the northeast Pacific: Seasonal variations and transport pathways of carbon monoxide, J.

825 Geophys. Res., 109(D23), D23S07, doi:10.1029/2003JD004402, 2004.

Lin, J.-T., McElroy, M. B., and Boersma, K. F.: Constraint of anthropogenic NO_x emissions in China from different sectors: a new methodology using multiple satellite retrievals, Atmos. Chem. Phys., 10, 63–78, doi:10.5194/acp-10-63-2010, 2010.

Martin, R. V., Jacob, D. J., Chance, K., Kurosu, T. P., Palmer, P. I., and Evans, M. J.: Global inventory of nitro-

830 gen oxide emissions constrained by space-based observations of NO_2 columns, J. Geophys. Res., 108(D17), 4537, doi:10.1029/2003JD003453, 2003.

Martin, R. V., Sioris, C. E., Chance, K. V., Ryerson, T. B., Bertram, T. H.,Woolridge, P. J., Cohen, R. C., Neuman, J. A., Swanson, A., and Flocke, F. M.: Evaluation of space-based constraints on nitrogen oxide emissions with regional aircraft measurements over and downwind of eastern North America, J. Geophys.

835 Res., 111, D15308, doi:10.1029/2005JD006680, 2006.

Martini, M., Allen, D. J., Pickering, K. E., Stenchikov, G. L., Richter, A., Hyer, E. J. and Loughner, C. P.: The impact of North American anthropogenic emissions and lightning on long-range transport of trace gases and their export from the continent during summers 2002 and 2004, J. Geophys. Res., 116(D7), D07305, doi:10.1029/2010JD014305, 2011.

840 Munro, R., Eisinger, M., Anderson, C., Callies, J., Corpaccioli, E., Lang, R., Lefebvre, A., Livschitz, Y., and Albinana, A. P.: GOME-2 on MetOp, in: Proc. of The 2006 EUMETSAT Me- teorological Satellite Conference, Helsinki, Finland, 12–16 June 2006, EUMETSAT, p. 48, 2006.

Nolin, A., Armstrong, R. L., and Maslanik, J.: Near Real-Time SSM/I EASE-Grid Daily Global Ice Concentration and Snow Extent, Jan to Mar 2004 (updated daily), Boulder, CO, USA: National Snow and Ice Data

845 Center, Digital media, 1998.

Oman, L. D., Douglass, A. R., Ziemke, J.R., Rodriguez, J. M., Waugh, D. W., and Nielson, J. E.: The ozone response to ENSO in Aura satellite measursments and a chemistry-climate simulation, J. Geophys. Res.,118, 965976, doi:10.1029/2012JD018546, 2013, in press.

Parrish, D. D.: Intercontinental Transport and Chemical Transformation 2002 (ITCT 2K2) and Pacific Explo-

850 ration of Asian Continental Emission (PEACE) experiments: An overview of the 2002 winter and spring intensives, J. Geophys. Res., 109(D23), D23S01, doi:10.1029/2004JD004980, 2004.

Perring, A. E., Bertram, T. H., Farmer, D. K., Wooldridge, P. J., Dibb, J., Blake, N. J., Blake, D. R., Singh, H. B., Fuelberg, H., Diskin, G., Sachse, G. and Cohen, R. C.: The production and persistence of $\Sigma RONO_2$ in the Mexico City plume, Atmos. Chem. Phys., 10(15), 7215–7229, doi:10.5194/acp-10-7215-2010, 2010.

855   Pickering, K. E., Wang, Y., Tao, W.-K., Price, C. and Müller, J.-F.: Vertical distributions of lightning NOx for use in regional and global chemical transport models, J. Geophys. Res., 103(D23), 31203–31216, doi:10.1029/98JD02651, 1998.

Price, C. and Rind, D.: A simple lightning parameterization for calculating global lightning distributions, J. Geophys. Res., 97, 9919–9933, 1992.

860   Price, C., Penner, J., and Prather, M.: NOx from lightning, Part I: Global distribution based on lightning physics, J. Geophys. Res., 102, 5929–5941, 1997.

Reidmiller, D. R., Jaffe, D. A., Chand, D., Strode, S., Swartzendruber, P., Wolfe, G. M. and Thornton, J. A.: Interannual variability of long-range transport as seen at the Mt. Bachelor observatory, Atmos. Chem. Phys., 9(2), 557–572, 2009.

865   Richter, A. and J.P. Burrows, Retrieval of Tropospheric NO2 from GOME Measurements, Adv. Space Res., 29(11) ,1673-1683, 2002 .

Richter, A., Burrows, J. P., Nusz, H., Granier, C. and Niemeier, U.: Increase in tropospheric nitrogen dioxide over China observed from space, Nature, 437(7055), 129–132, doi:10.1038/nature04092, 2005.

Rienecker, M. M., Suarez, M. J., Gelaro, R., Todling, R., Bacmeister, J., Liu, E., Bosilovich, M. G., Schubert, 870   S. D., Takacs, L., Kim, G.-K., Bloom, S., Chen, J., Collins, D., Conaty, A., da Silva, A., Gu, W., Joiner, J., Koster, R. D., Lucchesi, R., Molod, A., Owens, T., Pawson, S., Pegion, P., Redder, C. R., Reichle, R., Robertson, F. R., Ruddick, A. G., Sienkiewicz, M. and Woollen, J.: MERRA: NASA's Modern-Era Retrospective Analysis for Research and Applications, J. Climate, 24(14), 3624–3648, doi:10.1175/JCLI-D-11-00015.1, 2011.

875   Richter, A. and Burrows, J.P.: Retrieval of Tropospheric NO2 from GOME Measurements, Adv. Space Res., 29(11) ,1673-1683, 2002

Richter, A., Burrows, J. P., Nüß, H., Granier, C, Niemeier, U.: Increase in tropospheric nitrogen dioxide over China observed from space, Nature, 437, 129-132, doi: 10.1038/nature04092, 2005

Russell, A. R., Valin, L. C., Bucsela, E. J., Wenig, M. O., and Cohen, R. C.: Space-based Constraints on Spatial 880   and Temporal Patterns of NO_x Emissions in California, 2005–2008, Environ. Sci. Technol., 44, 3608–3615, doi:10.1021/es903451j, 2010.

Russell, A. R., Valin, L. C. and Cohen, R. C.: Trends in OMI NO_2 observations over the United States: effects of emission control technology and the economic recession, Atmos. Chem. Phys., 12(24), 12197–12209, doi:10.5194/acp-12-12197-2012, 2012.

885   Shindell, D. and Faluvegi, G.: Climate response to regional radiative forcing during the twentieth century, Nat. Geosci., 2(4), 294–300, doi:10.1038/ngeo473, 2009.

Singh, H. B., Brune, W. H., Crawford, J. H., Flocke, F. and Jacob, D. J.: Chemistry and transport of pollution over the Gulf of Mexico and the Pacific: spring 2006 INTEX-B campaign overview and first results, Atmos. Chem. Phys., 9(7), 2301–2318, 2009.

890   Sneep, M., de Haan, J. F., Stammes, P., Wang, P., Vanbauce, C., Joiner, J., Vasilkov, A. P. and Levelt, P. F.: Three-way comparison between OMI and PARASOL cloud pressure products, J. Geophys. Res., 113(D15), D15S23, doi:10.1029/2007JD008694, 2008.

Solomon, S., Qin, D., Manning, M., Alley, R. B., Berntsen, T., Bindoff, N. L., Chen, Z., Chidthaisong, A., Gregory, J. M., Hegerl, G. C., Heimann, M., Hewitson, B., Hoskins, B. J., Joos, F., Jouzel, J., Kattsov, V.,

895   Lohmann, U., Matsuno, T., Molina, M., Nicholls, N., Overpeck, J., Raga, G., Ramaswamy, V., Ren, J., Rusticucci, M., Somerville, R., Stocker, T. F., Whetton, P., Wood, R. A., and Wratt, D.: Technical Summary. In: Climate Change 2007: The Physical Science Basis. Contribution of Working Group I to the Fourth Assessment Report of the Intergovernmental Panel on Climate Change [Solomon, S., D. Qin, M. Manning, Z. Chen, M. Marquis, K.B. Averyt, M. Tignor and H.L. Miller (eds.)]. Cambridge University Press, Cambridge, United Kingdom and New York, NY, USA., 2007.

900

Stammes, P., Sneep, M., de Haan, J. F., Veefkind, J. P., Wang, P. and Levelt, P. F.: Effective cloud fractions from the Ozone Monitoring Instrument: Theoretical framework and validation, J. Geophys. Res., 113(D16), D16S38, doi:10.1029/2007JD008820, 2008.

Strahan, S. E., Duncan, B. N. and Hoor, P.: Observationally derived transport diagnostics for the lowermost
905   stratosphere and their application to the GMI chemistry and transport model, Atmos. Chem. Phys., 7(9), 2435–2445, 2007.

Thornton, J. A., Wooldridge, P. J., and Cohen, R. C.: Atmospheric NO2: In Situ Laser-Induced Fluorescence Detection at Parts per Trillion Mixing Ratios, Anal. Chem. 72, 528–539, 2000.

Vasilkov, A., Joiner, J., Spurr, R., Bhartia, P. K., Levelt, P. and Stephens, G.: Evaluation of the OMI cloud
910   pressures derived from rotational Raman scattering by comparisons with other satellite data and radiative transfer simulations, J. Geophys. Res., 113(D15), D15S19, doi:10.1029/2007JD008689, 2008.

Vasilkov, A. P., Joiner, J., Oreopoulos, L., Gleason, J. F., Veefkind, P., Bucsela, E., Celarier, E. A., Spurr, R. J. D. and Platnick, S.: Impact of tropospheric nitrogen dioxide on the regional radiation budget, Atmos. Chem. Phys., 9(17), 6389–6400, 2009.

915   Walker, T. W., Martin, R. V., van Donkelaar, A., Leaitch, W. R., MacDonald, A. M., Anlauf, K. G., Cohen, R. C., Bertram, T. H., Huey, L. G., Avery, M. A., Weinheimer, A. J., Flocke, F. M., Tarasick, D. W., Thompson, A. M., Streets, D. G. and Liu, X.: Trans-Pacific transport of reactive nitrogen and ozone to Canada during spring, Atmos. Chem. Phys., 10(17), 8353–8372, doi:10.5194/acp-10-8353-2010, 2010.

Wang, Y., Choi, Y., Zeng, T., Ridley, B., Blake, N., Blake, D. and Flocke, F.: Late-spring increase
920   of trans-Pacific pollution transport in the upper troposphere, Geophys. Res. Lett., 33(1), L01811, doi:10.1029/2005GL024975, 2006.

Wild, O., Prather, M. J., and Akimoto, H.: Indirect long-term global radiative cooling from NOx emissions, Geophys. Res. Lett., 28, 1719-1722, 2001.

Witte, J. C., Schoeberl, M. R., Douglass, A. R., Gleason, J. F., Krotkov, N. A., Gille, J. C., Pickering, K.
925   E. and Livesey, N.: Satellite observations of changes in air quality during the 2008 Beijing Olympics and Paralympics, Geophys. Res. Lett., 36(17), L17803, doi:10.1029/2009GL039236, 2009.

Zhang, L., Jacob, D. J., Boersma, K. F., Jaffe, D. A., Olson, J. R., Bowman, K. W., Worden, J. R., Thompson, A. M., Avery, M. A. and Cohen, R. C.: Transpacific transport of ozone pollution and the effect of recent Asian emission increases on air quality in North America: an integrated analysis using satellite, aircraft,
930   ozonesonde, and surface observations, Atmospheric Chemistry and Physics Discussions, 8(2), 8143–8191, 2008.

Ziemke, J. R., Chandra, S. and Bhartia, P. K.: "Cloud slicing": A new technique to derive upper tropospheric ozone from satellite measurements, J. Geophys. Res. (1984-2012), 106(D9), 9853–9867, 2001.

Ziemke, J. R., Chandra, S., and Bhartia, P. K.: Upper tropospheric ozone derived from the cloud

935   slicing technique: Implications for large-scale convection, J. Geophys. Res., 108(D13), 4390, doi:10.1029/2002JD002919, 2003.

Ziemke, J. R. Chandra, S., and Bhartia, P. K.: A 25-year data record of atmospheric ozone in the Pacific from Total Ozone Mapping Spectrometer (TOMS) cloud slicing: Implications for ozone trends in the stratosphere and troposphere, J. Geophys. Res., 110(D15), D15105, doi:10.1029/2004JD005687, 2005.

940   Ziemke, J. R., Joiner, J., Chandra, S., Bhartia, P. K., Vasilkov, A., Haffner, D. P., Yang, K., Schoeberl, M. R., Froidevaux, L. and Levelt, P. F.: Ozone mixing ratios inside tropical deep convective clouds from OMI satellite measurements, Atmos. Chem. Phys., 9(2), 573–583, 2009.

Ziemke, J. R., Chandra, S., Oman, L. D. and Bhartia, P. K.: A new ENSO index derived from satellite measurements of column ozone, Atmos. Chem. Phys., 10(8), 3711–3721, 2010.

945   Ziemke, J. R., Chandra, S., Labow, G. J., Bhartia, P. K., Froidevaux, L. and Witte, J. C.: A global climatology of tropospheric and stratospheric ozone derived from Aura OMI and MLS measurements, Atmos. Chem. Phys., 11(17), 9237–9251, doi:10.5194/acp-11-9237-2011, 2011.

Ziemke, J. R. and Chandra, S.: Development of a climate record of tropospheric and stratospheric column ozone from satellite remote sensing: evidence of an early recovery of global stratospheric ozone, Atmos. Chem.

950   Phys., 12(13), 5737–5753, doi:10.5194/acp-12-5737-2012, 2012.

Zhang, Q., Streets, D. G., He, K.,Wang, Y., Richter, A., Burrows, J. P., Uno, I., Jang, C. J., Chen, D., Yao, Z., and Lei, Y.: NO_x emission trends for China, 1995–2004: The view from the ground 15 and the view from space, J. Geophys. Res., 112, D22306, doi:10.1029/2007jd008684, 2007.

29

(a) Measurements at Cloudy Scenes

Top of Atmosphere (TOA)

Cloud scene
pressure

Ground

(b) Observed Column vs Pressure

0

TOA

Pressure(hPa)

P1

ΔP

P2

ΔVCD

Ground

~1013

Above-cloud NO_2 VCD

(c) Slope to NO_2 VMR

0

TOA

NO_2 VMR

$= \dfrac{\Delta VCD}{\Delta P}$ * constant

Pressure (hPa)

P1

Pressure
Range

P2

Confidence
Interval
Of NO_2 VMR

Ground

~1013

NO_2 VMR

(d) Extrapolation for Stratospheric Column NO_2

0

TOA

Tropopause
Pressure

Ground

~1013

Strat NO_2 VCD
(above-tropopause column)

Above-cloud NO_2 VCD

Fig. 1. Schematic view of the cloud slicing technique (not to scale): (a) two above-cloud NO_2 column measurements at different cloud scene pressures (blue: column with lower scene pressure; and red: column with higher scene pressure); (b) the measurements shown on a pressure-column coordinate plane; (c) NO_2 VMR derived from the slope of above-cloud NO_2 VCD versus cloud scene pressure with confidence interval (horizontal error bar) and pressure range (vertical error bar); (d) stratospheric column NO_2 derived by extrapolating the linear fit to the tropopause.

30
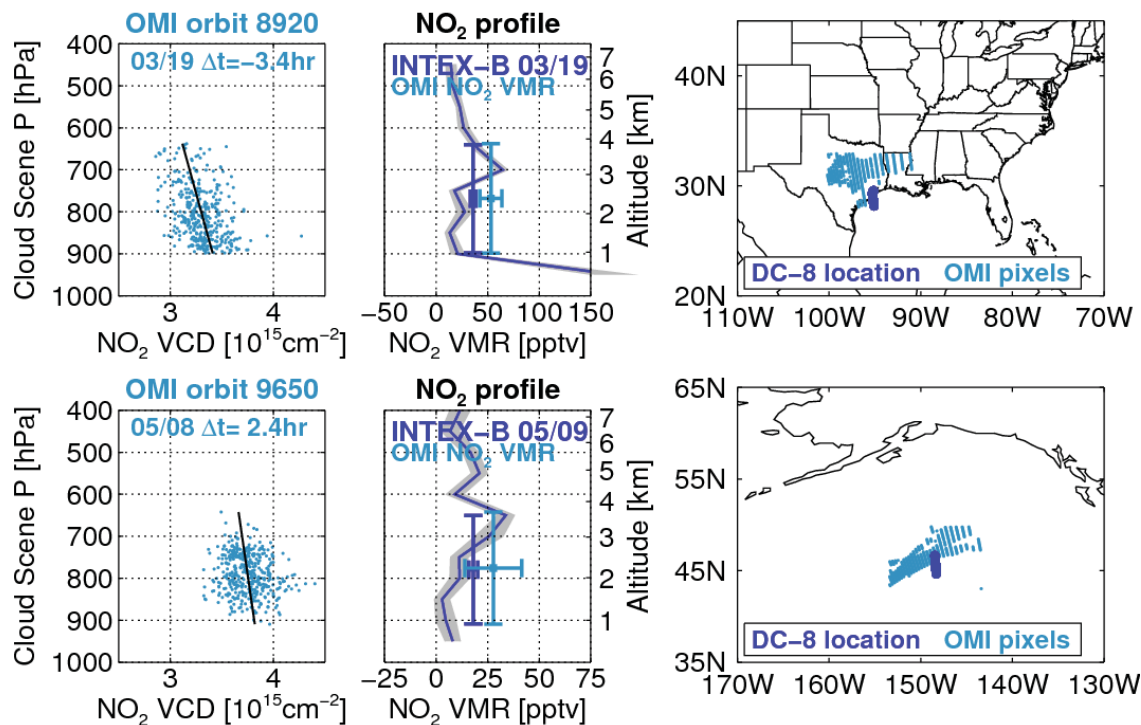
Fig. 2. Examples of relatively good agreement between OMI cloud slicing VMRs and INTEX-B NO_2 profiles near Houston, Texas, US (top row) and the northeastern Pacific (bottom row). In each example, left: OMI above-cloud NO_2 column versus cloud scene pressure (similar to Fig. 1b); center: INTEX-B NO_2 profiles (dark blue line), INTEX-B NO_2 VMR averaged over the OMI pressure range (dark blue square with error bars), and OMI-derived NO_2 VMR (light blue square with error bars); right: locations of OMI and INTEX-B aircraft measurements.
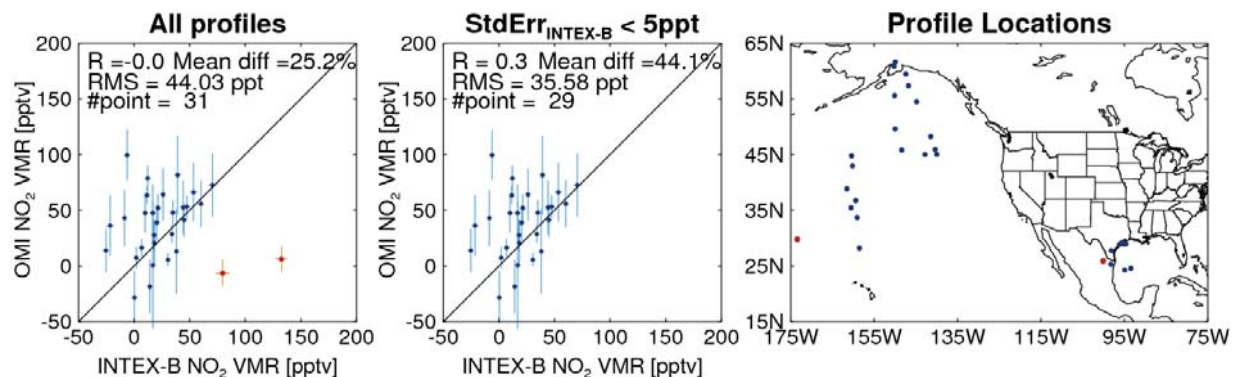
Fig. 3. Scattergram of INTEX-B and OMI cloud slicing NO_2 VMRs; Left: all available collocations of INTEX-B and OMI NO_2 VMR; Middle: collocations where the INTEX-B standard error of the mean < 5 pptv; Right: locations of the profiles. Red shows cases where the INTEX-B standard error of the mean > 5pptv.

31
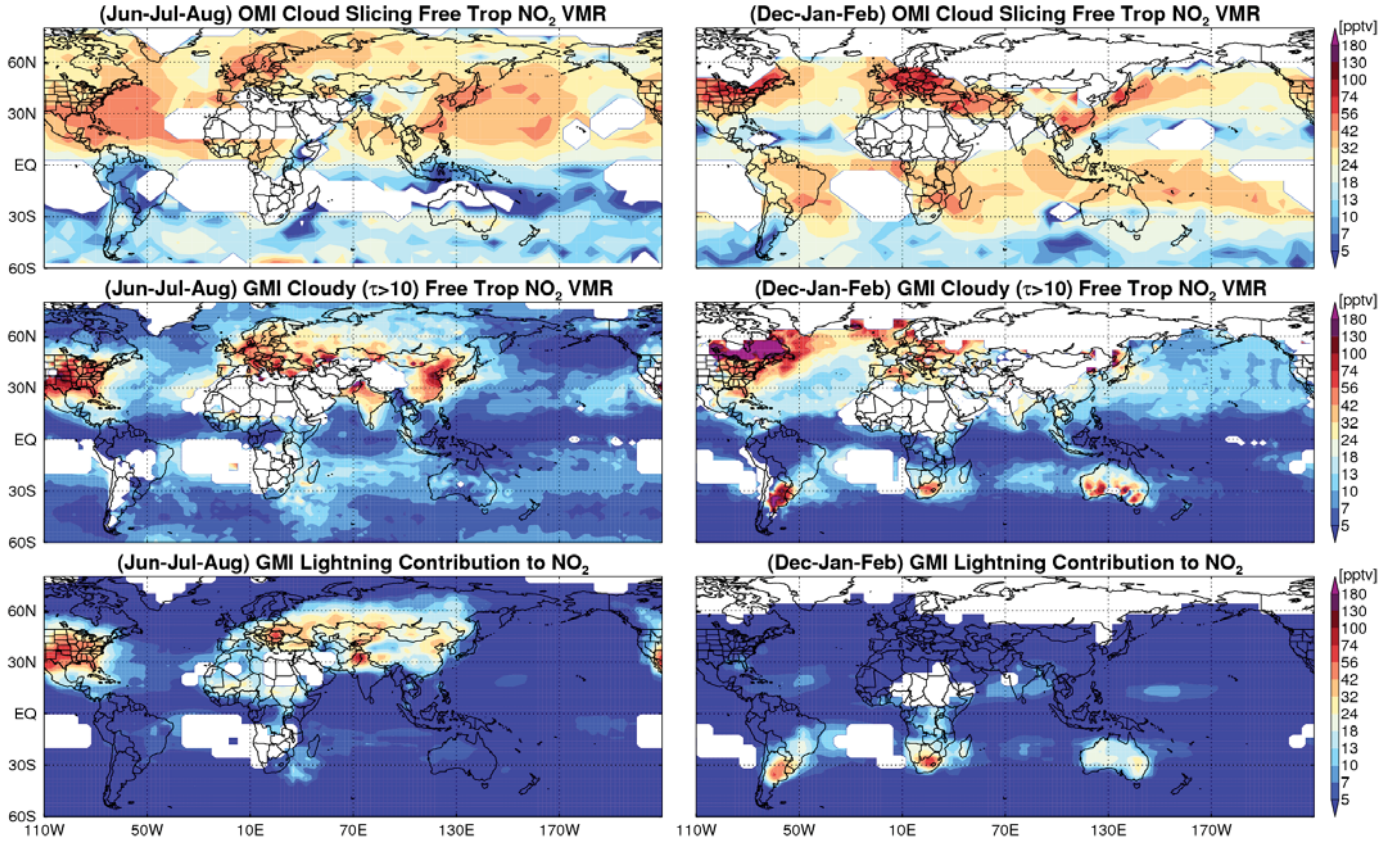
Fig. 4. For Jun-Aug (left column) and Dec-Feb (right column) averages over 2005-2007; First row: Climatology of free tropospheric NO_2 VMR; Second row: cloudy ($\tau > 10$) GMI free tropospheric NO_2 VMR; Third row: GMI lightning contribution to the free tropospheric NO_2 VMRs.
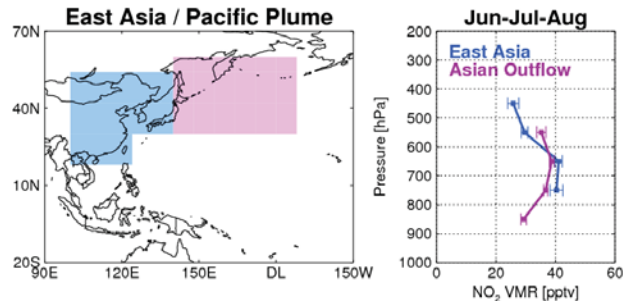
Fig. 5. Left: sampling areas for profiles over East Asia (blue) and its outflow region (purple); right: NO_2 profiles over East Asia (blue) and its outflow region (purple) with standard errors in summer for 2005–2007.
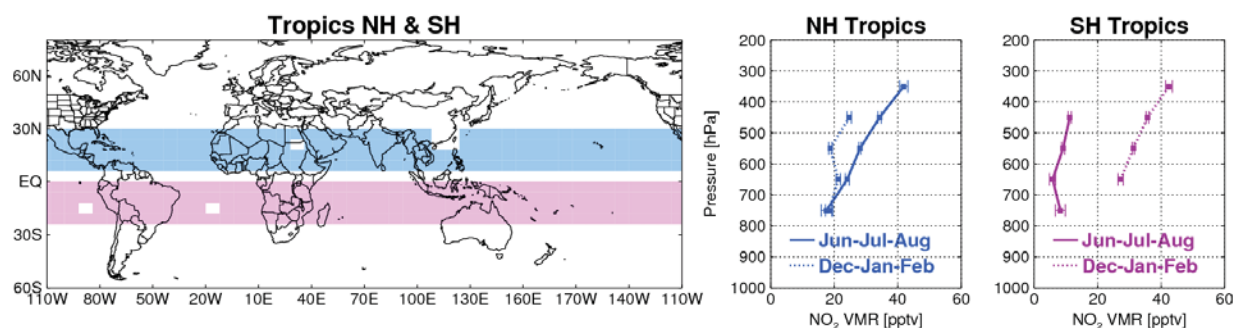
Fig. 6. Left: sampling areas for profiles over tropics of NH (blue) and SH (purple); center: NO₂ profiles over NH tropics for Jun-Aug (blue solid line) and Dec-Feb (blue dotted line) with standard errors; right: NO₂ profiles over SH tropics for Jun-Aug (purple solid line) and Dec-Feb (purple dotted line) for 2005–2007.
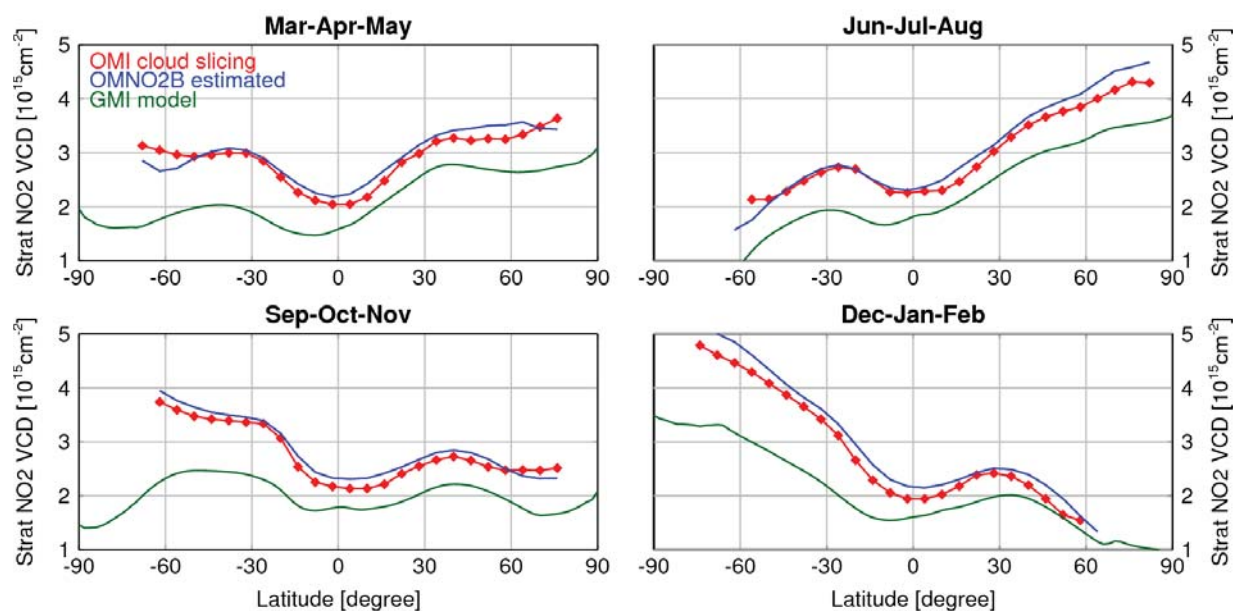
Fig. 7. Seasonal, zonal mean of various estimates of stratospheric column NO₂ averaged over 2005–2007.

33
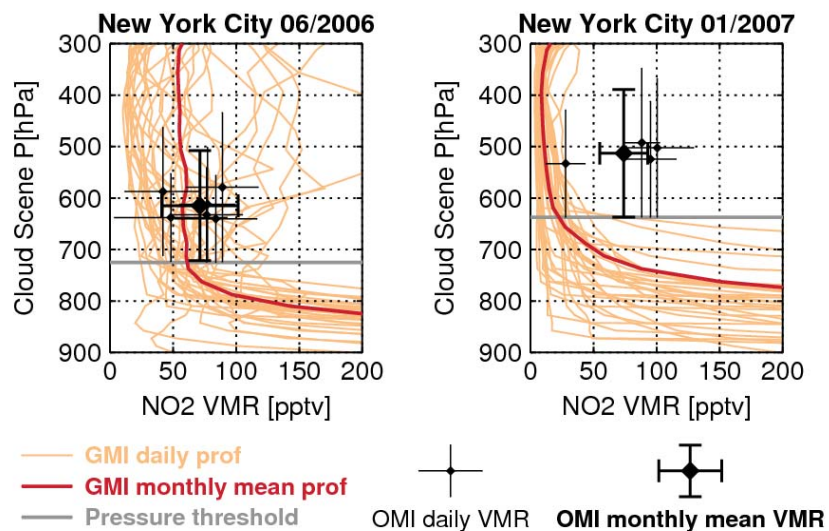
Fig. A1. Example of calculating a climatological free tropospheric NO_2 VMR for a grid box that encompasses New York City; Left: May 2005; Right: January 2007; Lines show daily (orange) and monthly mean (red) GMI NO_2 profiles. Grey horizontal lines show the pressure threshold above which the NO_2 vertical gradient is $<$ 0.33 pptv/hPa.
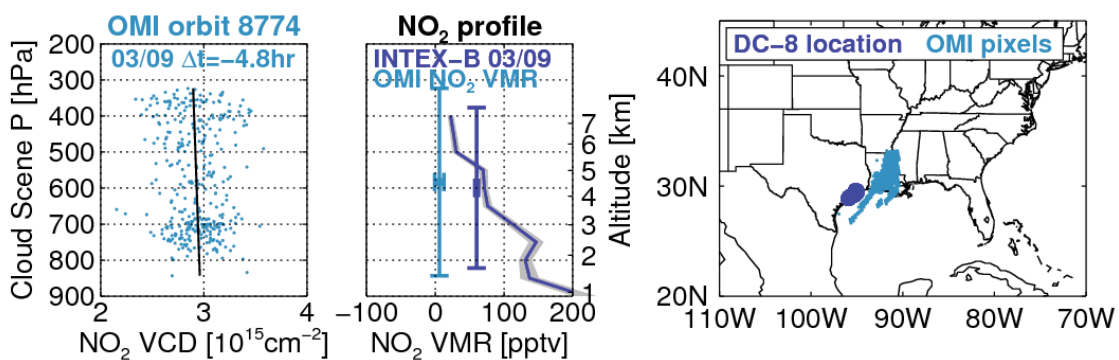
Fig. B1. Similar to Fig. 2, but showing a case with a discrepancy between satellite and aircraft measurements, possibly due to poor collocation, with INTEX-B measurements near Houston, Texas, US and OMI measurements over Louisiana, US.

34
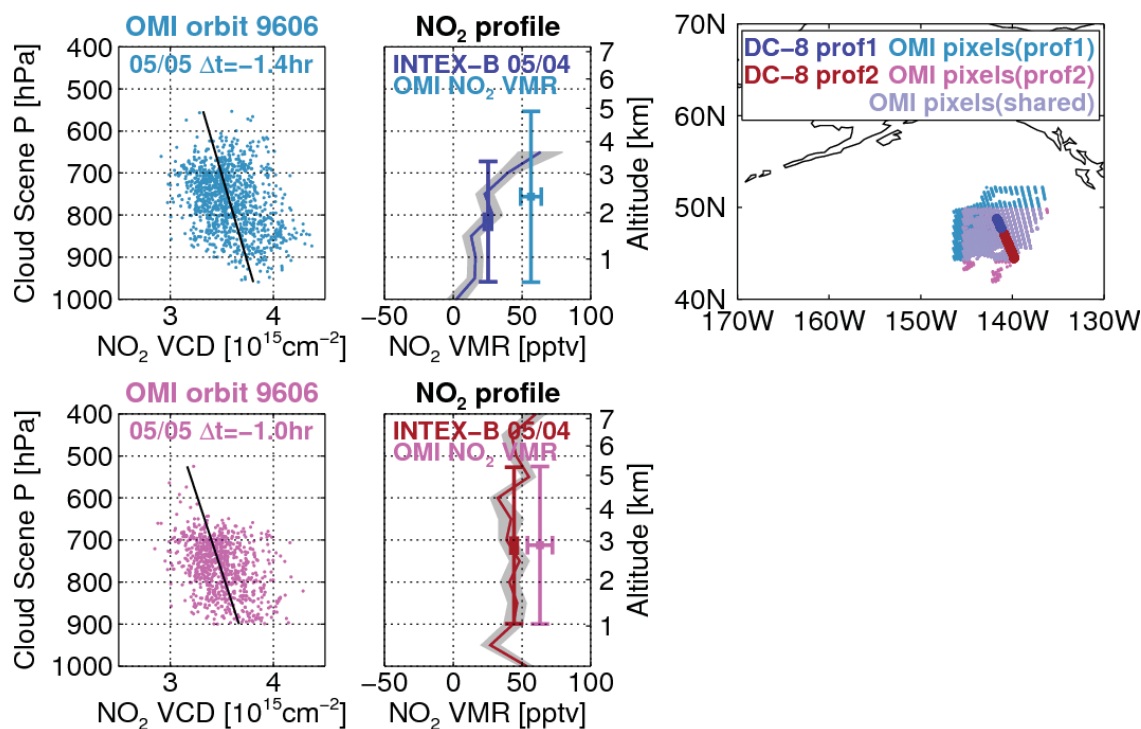
Fig. B2. Similar to Fig. B1, showing another example over the northeastern Pacific with a discrepancy between satellite and aircraft data apparently due to small-scale spatial variations in the INTEX-B NO_2 profiles.
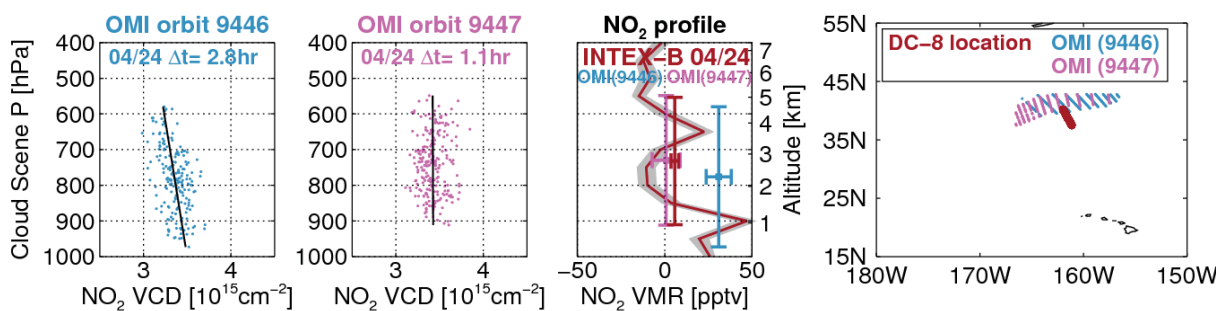
Fig. B3. Similar to Fig. 2, but showing an example of variation in OMI NO_2 VMRs over two adjacent orbits (1.5 hour time difference) at the same location north of Hawaii, US.
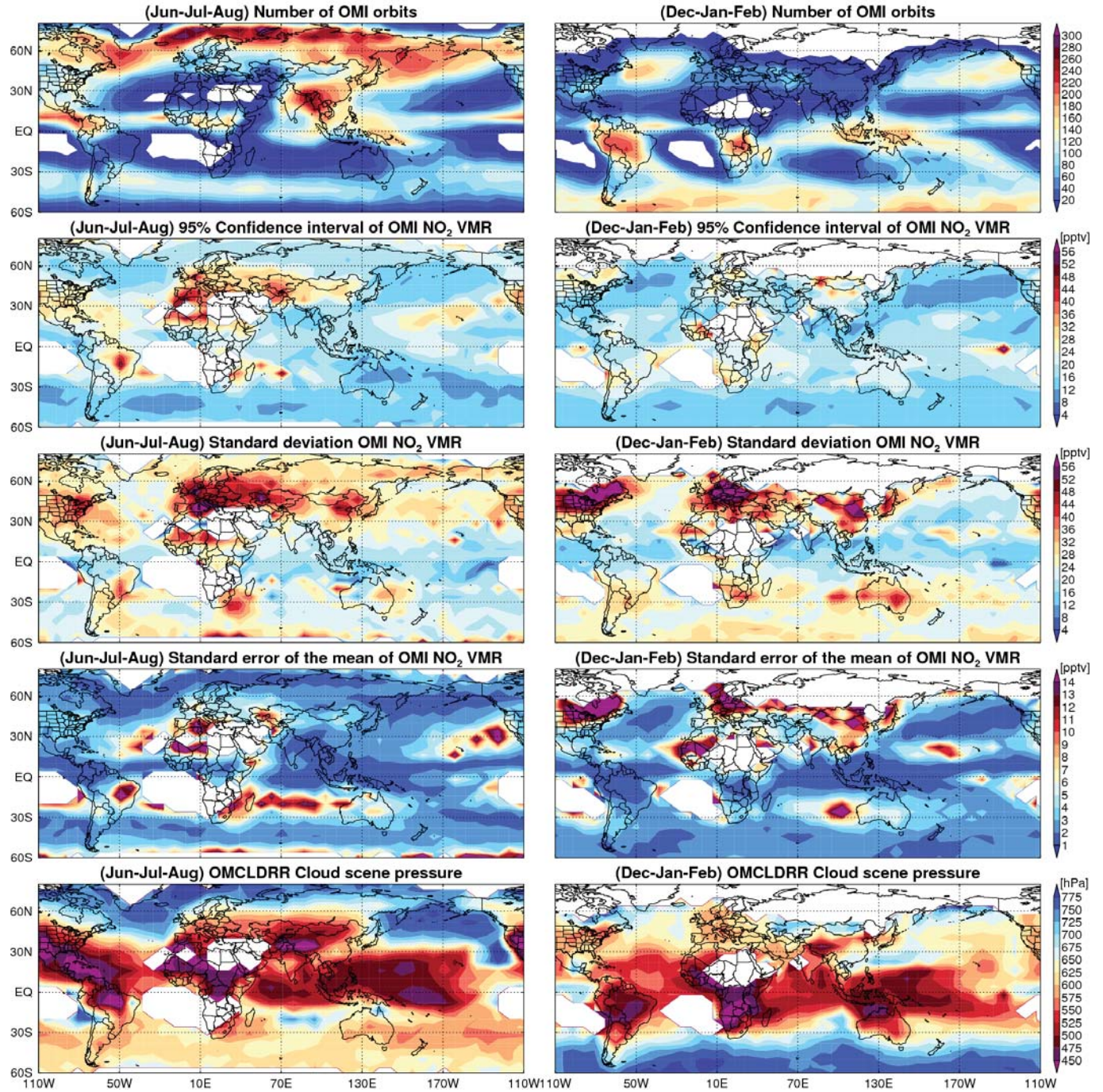
Fig. C1. Left: Jun-Aug and Right: Dec-Feb averages over 2005-2007: First row: Number of OMI overpasses used to derive NO$_2$ VMR climatology; Second row: 95% confidence interval of NO$_2$ VMRs; Third row: Standard deviation of NO$_2$ VMRs; Fourth row: Standard error of the mean of NO$_2$ VMRs; Fifth row: mean OMCLDRR cloud scene pressures used to compute the NO$_2$ VMR climatology.
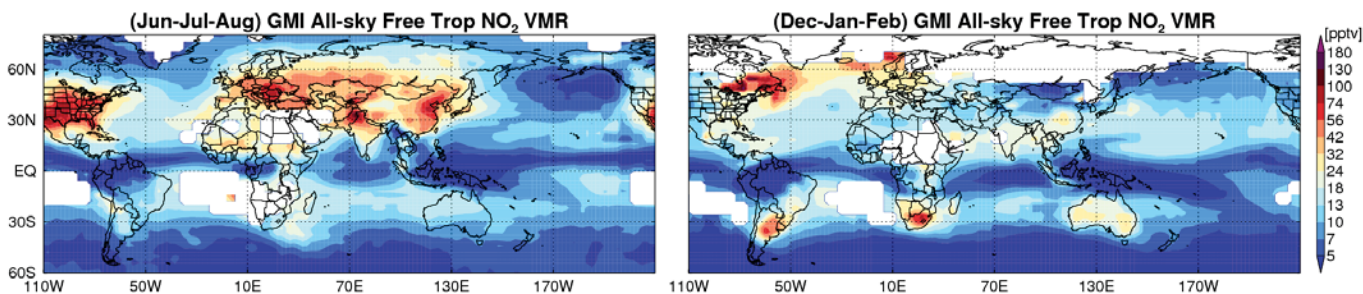
Fig. C2. GMI all-sky free tropospheric NO$_2$ for Jun-Aug (left) and Dec-Feb (right) averages over 2005-2007.
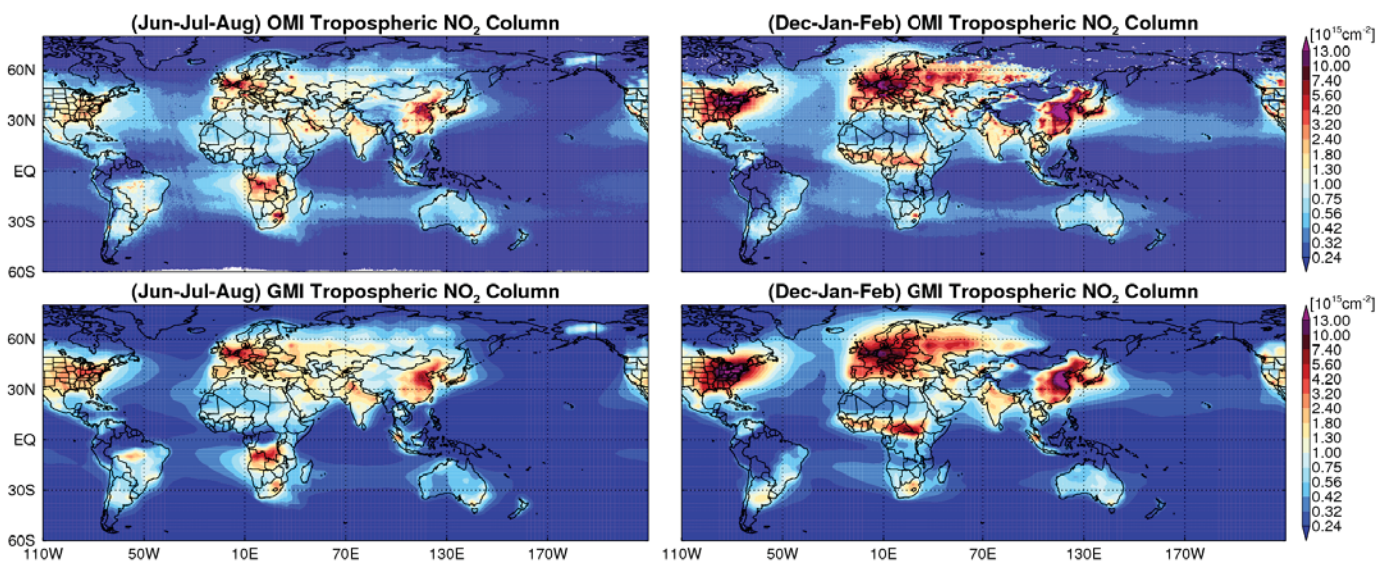

Fig. C3. For Jun-Aug (left column) and Dec-Feb (right column) averages over 2005-2007; Top: OMI tropospheric column NO$_2$; Bottom: GMI tropospheric column NO$_2$.
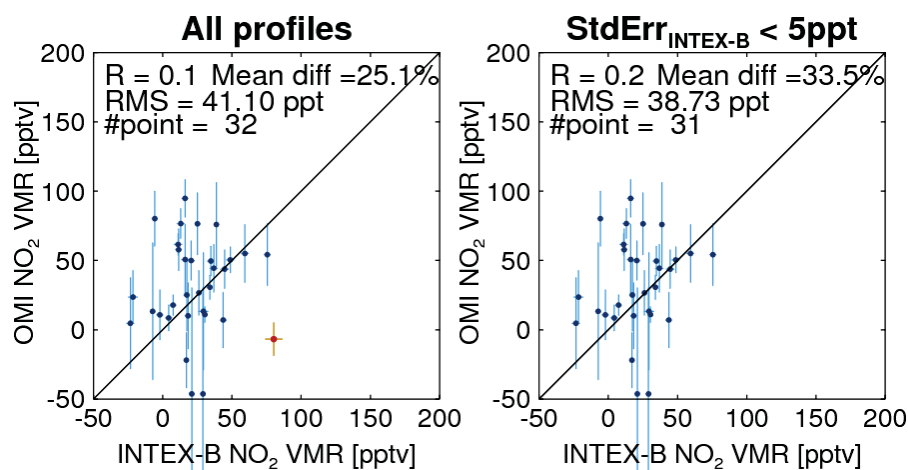
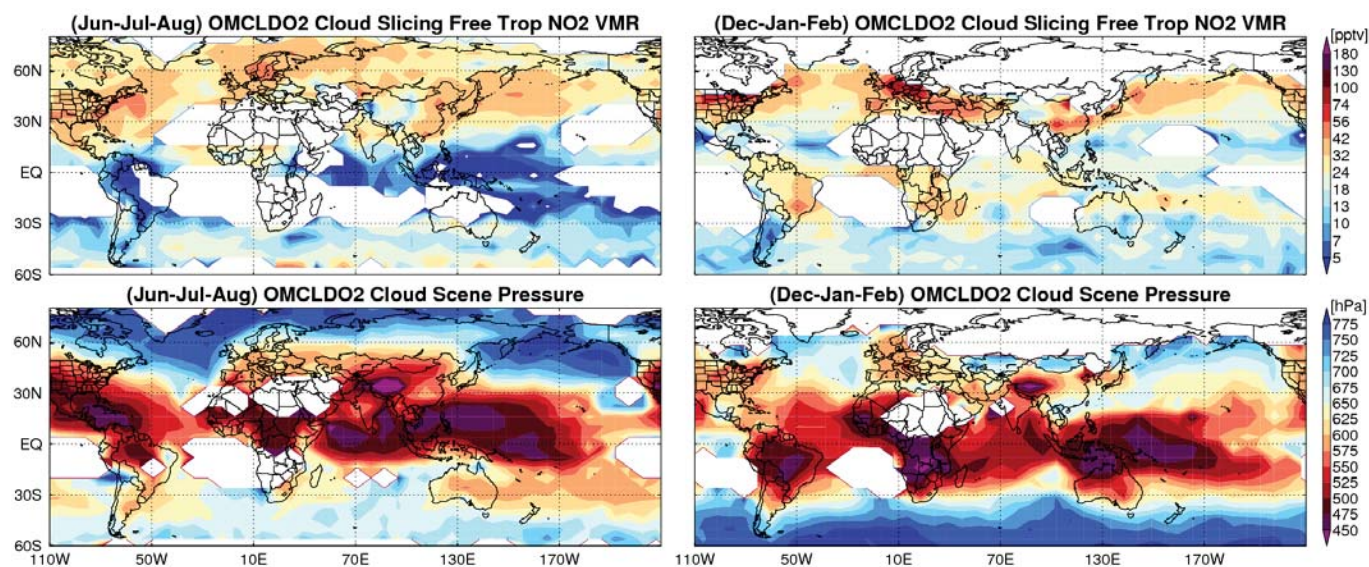**Fig. D1.** Similar to Fig. 3 but using OMCLDO2 data.

Fig. D2. For Jun.-Aug. (left) and Dec.-Feb. (right) averaged over 2005-2007, Top: Global maps of NO_2 VMR calculated using OMCLDO2 cloud parameters; Bottom: Mean cloud scene pressures from OMCLDO2.

Table 1. OMI data filtering criteria for cloud slicing approach.

Individual pixel	Cloud radiance fraction (f_r)	> 0.9
	UV aerosol index	< 1.0
	Solar zenith angle (SZA)	$< 80°$
	Snow and ice flag	$= 0$ (not affected by snow/ice)
Pixel collection	Number of OMI Pixels	> 30
	Range of cloud effective scene pressure (P_{scene})	> 200 hPa
	Standard deviation of cloud effective scene pressure (P_{scene})	> 35 hPa
	Gradient of NO$_2$ VMR over pressure (dVMR/dP)*	< 0.33 pptv / hPa

*Obtained from INTEX-B or GMI profiles